



# On the formation and early evolution of soot in turbulent nonpremixed flames

Fabrizio Bisetti<sup>a,\*</sup>, Guillaume Blanquart<sup>b</sup>, Michael E. Mueller<sup>c</sup>, Heinz Pitsch<sup>d</sup>

<sup>a</sup> Clean Combustion Research Center, King Abdullah University of Science and Technology, Thuwal 23955, Saudi Arabia

<sup>b</sup> Department of Mechanical Engineering, California Institute of Technology, Pasadena, CA 91125, USA

<sup>c</sup> Department of Mechanical Engineering, Stanford University, Stanford, CA 94305, USA

<sup>d</sup> Institut für Technische Verbrennung, RWTH Aachen University, 52056 Aachen, Germany

## ARTICLE INFO

### Article history:

Received 24 November 2010

Received in revised form 25 May 2011

Accepted 26 May 2011

Available online 25 June 2011

### Keywords:

Soot

Direct Numerical Simulation

Turbulent nonpremixed combustion

Polycyclic Aromatic Hydrocarbons

Particulate morphology

*n*-heptane

## ABSTRACT

A Direct Numerical Simulation (DNS) of soot formation in an *n*-heptane/air turbulent nonpremixed flame has been performed to investigate unsteady strain effects on soot growth and transport. For the first time in a DNS of turbulent combustion, Polycyclic Aromatic Hydrocarbons (PAH) are included via a validated, reduced chemical mechanism. A novel statistical representation of soot aggregates based on the Hybrid Method of Moments is used [M.E. Mueller, G. Blanquart, H. Pitsch, *Combust. Flame* 156 (2009) 1143–1155], which allows for an accurate state-of-the-art description of soot number density, volume fraction, and morphology of the aggregates. In agreement with previous experimental studies in laminar flames, Damköhler number effects are found to be significant for PAH. Soot nucleation and growth from PAH are locally inhibited by high scalar dissipation rate, thus providing a possible explanation for the experimentally observed reduction of soot yields at increasing levels of mixing in turbulent sooting flames. Furthermore, our data indicate that soot growth models that rely on smaller hydrocarbon species such as acetylene as a proxy for large PAH molecules ignore or misrepresent the effects of turbulent mixing and hydrodynamic strain on soot formation due to differences in the species Damköhler number. Upon formation on the rich side of the flame, soot is displaced relative to curved mixture fraction iso-surfaces due to differential diffusion effects between soot and the gas-phase. Soot traveling towards the flame is oxidized, and aggregates displaced away from the flame grow primarily by condensation of PAH on the particle surface. In contrast to previous DNS studies based on simplified soot and chemistry models, surface reactions are found to contribute barely to the growth of soot, for nucleation and condensation processes occurring in the fuel stream are responsible for the most of soot mass generation. Furthermore, the morphology of the soot aggregates is found to depend on the location of soot in mixture fraction space. Aggregates having the largest primary particles populate the region closest to the location of peak soot growth. On the contrary, the aggregates with the largest number of primary particles are located much further into the fuel stream.

© 2011 The Combustion Institute. Published by Elsevier Inc. All rights reserved.

## 1. Introduction

Soot particles are formed during rich combustion of fossil fuels in technical devices such as internal combustion engines, jet engines, and coal burners [1]. Soot is an undesirable product of combustion. The carbon mass tied up in particulates is a combustion inefficiency since the full chemical potential of the fuel is not realized via complete conversion of carbon to carbon dioxide. Soot particles are also recognized as an important cause of health complications [2] such as pulmonary conditions and cancer. Lighty et al. [3] highlight that there exists accumulating evidence suggesting that the mass concentration of soot particles is not the most appropriate measure of health hazard. Particle surface area, number of ultrafine particles, morphology, and particle-bound

compounds such as transition metals are considerably more important in causing adverse health effects.

Despite the well-known negative effects of soot on human health and the environment, the formation and evolution of particulates in turbulent flames typical of technical devices remain not well understood. Areas of limited knowledge include the role of turbulence in controlling soot formation, the importance of soot preferential diffusion during turbulent mixing, the leading soot growth processes, and the mechanisms of soot oxidation. These gaps hinder the development of predictive models that can be used with advanced computational approaches such as Large Eddy Simulation (LES).

A number of past and recent studies have investigated the interaction between soot formation and transport by focusing on the effect of strain rate on PAH concentrations in sooting and non-sooting laminar counterflow flames. Du et al. [4] found a critical strain rate at which PAH fluorescence becomes negligible. This

\* Corresponding author. Fax: +966 2 802 0123.

E-mail address: [fabrizio.bisetti@kaust.edu.sa](mailto:fabrizio.bisetti@kaust.edu.sa) (F. Bisetti).

critical strain rate is significantly lower compared to the flame extinction strain rate and can be interpreted as an extinction limit for soot precursors. Similar results were reported in methane/air flames by Böhm et al. [5] and in acetylene/air flames by Yamamoto et al. [6].

The analysis of the effects of turbulent mixing and local scalar dissipation rate on turbulent sooting flames is a highly complex task and far fewer experimental or numerical studies are available than for laminar flames. Kent and Bastin [7] established that soot volume fraction decreases with increasing strain rate. They note that peak soot values decrease linearly with decreasing flame time at low flow rates (low strain), while at the highest flow rates (high strain), peak soot values drop sharply. More recently, Qamar et al. [8] performed laser-induced incandescence (LII) measurements on three different turbulent nonpremixed flame configurations with varying global mixing rates. They confirmed that increasing mixing rates reduces soot volume fraction and further report that the flame with the lowest values of instantaneous, local scalar dissipation rate also shows the highest levels of soot volume fraction.

A definitive explanation for the reduction of soot in flames with increasing global mixing rates is still missing and various mechanisms have been postulated. A preferred explanation relates turbulent mixing to reduced soot residence times [9], fuel dilution, and localized premixing. In this work, the role of PAH in controlling soot formation in turbulent flames is explored.

Over the past few years, a few DNS studies on soot formation in turbulent flames have been performed. Yoo and Im [9] studied the dynamics of soot formation in turbulent ethylene-air counterflow diffusion flames using Direct Numerical Simulation (DNS). A one-step hydrocarbon chemistry [10] and a simplified two-equation soot model [11] were used. They found that turbulence has a two-fold effect on soot volume fraction. Turbulence increases the global soot yield by increasing flame surface, and it inhibits particle growth by reducing the time soot spends in the high temperature flame region where growth is most intense.

Narayanan and Trounev [12] studied the occurrence of flame weakening, flame extinction, and soot leakage across the flame in a two-dimensional convection-driven turbulent wall-flame configuration using DNS. In order to make the simulation computationally tractable, they used a number of simplifications such as a one-step chemical reaction [10] and a two-equation semi-empirical soot model [13]. They concluded that enhanced radiation caused by soot results in frequent flame weakening events and subsequent soot mass leakage across the weakened flame. They also concluded that turbulent flames are more susceptible to radiation extinction than their laminar counterparts.

Recently, Lignell et al. [14,15] performed two DNS studies (2D and 3D) aimed at examining the effects of soot-flame interaction and soot transport in a temporally evolving mixing layer. They used a reduced ethylene/air mechanism obtained from a detailed propane mechanism [16] together with the semi-empirical soot model of Leung et al. [13]. In this soot model, nucleation and surface growth rates depend on temperature and the concentration of acetylene, while aromatic species do not contribute to soot growth. Consistent with previous modeling studies, the authors highlighted the role of differential diffusion between soot and the gas-phase in determining soot growth rates. They also correlated the direction of transport with soot volume fraction. They observed that the largest soot volume fraction occurs where soot particles move towards the flame sheet and grow by surface reactions. In agreement with previous DNS data obtained employing the same soot model [13], surface growth by acetylene is found to be the greatest contributor to soot growth.

The intent of the present work is to provide insight into the processes controlling soot formation and growth in turbulent flames, while considering state-of-the-art chemistry and soot models. A

two-dimensional turbulent nonpremixed flame subject to decaying isotropic turbulence is selected to make the simulation computationally tractable. This study distinguishes itself from previous work [9,14,15] by considering finite rate chemistry from fuel oxidation to the formation of Polycyclic Aromatic Hydrocarbons (PAH) and a detailed soot model based on elementary physical processes and rates [17] rather than using a semi-empirical approach [11,13]. Finite rate chemistry allows for the investigation of the effect of turbulent mixing on the formation and yield of key soot precursors such as acetylene and naphthalene. In addition, the morphology of soot particles is captured adequately since the soot model used is able to describe both small spherical particles and large aggregates. Furthermore, the soot model predicts both soot number density and volume fraction, accounting for the effects of persistent nucleation on the population of soot particles.

The paper is structured as follows. First, the physical models and numerical approach are presented in Section 2. Section 3 describes the initial conditions and computational setup. The results of the study are shown in Sections 4 and 5. The conclusions appear in Section 6.

## 2. Physical models and numerical methods

The following sections describe the numerical approach for solving the governing equations in the limit of low Mach number flows (Section 2.1), the reduced chemical mechanism (Section 2.2), and the soot model (Section 2.3).

### 2.1. Momentum and scalar transport equations

#### 2.1.1. Governing equations

The unsteady Navier-Stokes equations for continuity, momentum, temperature, and species mass fractions (e.g. [18, p. 2]) are used with simplifying assumptions valid in the limit of low Mach number combustion. Heating due to viscous dissipation, body forces, diffusion due to pressure gradients, and Soret and Dufour effects are neglected. Mass continuity is written as

$$\frac{\partial \rho}{\partial t} + \nabla \cdot (\rho \mathbf{u}) = 0, \quad (1)$$

where  $\mathbf{u} = (u, v)$  is the two-component velocity vector, and  $\rho$  is the mixture density. Conservation of momentum reads

$$\frac{\partial \rho \mathbf{u}}{\partial t} + \nabla \cdot (\rho \mathbf{u} \mathbf{u}) = -\nabla p + \nabla \cdot \boldsymbol{\tau}, \quad (2)$$

where  $p$  is pressure and

$$\boldsymbol{\tau} = \mu(\nabla \mathbf{u} + (\nabla \mathbf{u})^T) - \frac{2}{3}\mu(\nabla \cdot \mathbf{u})\mathbf{I}. \quad (3)$$

In Eq. (3),  $\mu$  is the dynamic viscosity and  $\mathbf{I}$  is the identity tensor. Transported scalars include species mass fractions, temperature, and selected statistical moments of the soot number density function (see Section 2.3). Assuming unity Lewis number for all species, a common assumption in turbulent nonpremixed combustion modeling, the transport equation for the mass fraction of species  $i$  is

$$\frac{\partial \rho Y_i}{\partial t} + \nabla \cdot (\rho Y_i \mathbf{u}) = \nabla \cdot (\rho D_{th} \nabla Y_i) + w_i \quad (1 \leq i \leq N), \quad (4)$$

where  $D_{th}$  is the mixture thermal diffusivity and  $w_i$  is the net production rate of species  $i$  by chemical reactions. Gas-phase Lewis number effects were investigated with the aid of flamelet solutions (see Appendix A). It was found that the simplified treatment of gas-phase species mass diffusion (unity Lewis number) has an impact on the overall soot volume fraction, but does not change the soot evolution process.

The transport equation for temperature is

$$c_p \left[ \frac{\partial T}{\partial t} + \nabla \cdot (\rho T \mathbf{u}) \right] = \nabla \cdot (\rho D_{th} c_p \nabla T) - \sum_i h_i w_i + \sum_i \rho D_{th} c_{p,i} \nabla T \cdot \nabla Y_i + \frac{dp_0}{dt} \quad (5)$$

where  $h_i$  is the enthalpy of formation of species  $i$  and  $c_p$  is the mixture specific heat at constant pressure. The last term on the r.h.s. of Eq. (5) accounts for changes in the background pressure since the DNS is performed at a constant volume.

The Navier–Stokes equations are complemented by the equation of state for an ideal gas

$$\rho = \rho(p_0, T, Y_i) = \frac{p_0 W}{RT}, \quad (6)$$

where  $R$  is the universal gas constant and  $W(Y_i)$  is the mixture molecular mass. The rate of change of  $p_0$  due to chemical reactions in a constant volume domain  $\Omega$  is obtained indirectly by imposing the following integral constraint on mass conservation

$$\frac{d}{dt} \int_{\Omega} \rho d\Omega = \frac{d}{dt} \int_{\Omega} \frac{p_0 W}{RT} d\Omega = 0. \quad (7)$$

All transport properties are mixture averaged and depend on temperature and mixture composition only [19].

The transport equation for selected moments is written as

$$\frac{\partial M}{\partial t} + \nabla \cdot (M \mathbf{u}) = -\nabla \cdot \mathbf{j}_M + \dot{M}, \quad (8)$$

where  $M$  is a moment of the soot number density function (representing the total soot number density, volume fraction, etc.),  $\mathbf{j}_M$  is its mass flux, and  $\dot{M}$  is its source term describing processes such as nucleation, coagulation, condensation, surface growth, and oxidation. Soot transport is characterized by a high Schmidt number (low diffusivity). Under standard atmospheric conditions, spherical particles with a diameter of 10 nm (resp. 100 nm) have a Schmidt number equal to 290 (resp.  $2.2 \times 10^4$ ) [20, p. 34]. Thus, the contribution of molecular diffusion to the mass flux is negligible and only thermophoretic effects are included as in Ref. [21]:

$$\mathbf{j}_M = -0.556 M \nu \frac{\nabla T}{T}. \quad (9)$$

The absence of soot mass fluxes due to negligible diffusion velocities results in significant differential diffusion effects between the gas-phase species and soot. As will be shown, those effects are much more important than differential diffusion effects amongst gas-phase species, which have been neglected.

A complete description of the moments and the source terms is provided later in Section 2.3.

### 2.1.2. Discretization

The transport equations are discretized on a homogeneous, structured, Cartesian mesh and solved with the finite difference method implemented in a parallel code using Message Passing Interface (MPI). The in-house code is called “NGA” and was developed at Stanford University. Details about the numerical methods are available in Desjardins et al. [22] and only a brief description is provided here.

Spatial transport of momentum is discretized with a centered second order operator on a staggered mesh. The spatial discretization of all species mass fractions and temperature relies on a third order BQUICK scheme [23] to ensure that the species mass fractions remain bounded between zero and one. The third order QUICK scheme of Leonard [24] is used for the transport of soot moments. Time integration proceeds with the iterative second order semi-implicit Crank–Nicolson scheme of Pierce and Moin [25]. In the present work, four sub-iterations were found sufficient to

reach second order accurate solutions and guarantee stability. At each time step, the chemical source terms for the species mass fractions and temperature are integrated implicitly at every computational node using the DVODE package [26] and are computed independently from transport.

The source terms  $\dot{M}_s$  in the transport equation of soot moments (Eq. (8)) are handled via time-splitting, in which one alternates between solving the transport equations without source terms and a system of ordinary differential equations modeling the soot processes. As pointed out by LeVeque and Yee [27], time-splitting is a convenient and robust approach to the time integration of hyperbolic conservation laws with stiff source terms. The second-order accurate Strang splitting [28] is adopted

$$M^{n+1} = S_{\psi}(h/2) S_f(h) S_{\psi}(h/2) M^n, \quad (10)$$

where  $h$  is the time advancement,  $S_{\psi}$  represents the numerical solution operator for the ODE system  $\partial M / \partial t = \dot{M}$ , and  $S_f(h)$  represents the numerical solution operator for the system of conservative equations without the source terms. In this work, the operator  $S_{\psi}(h)$  is approximated by a second order explicit Runge–Kutta method [29] with an appropriate number of sub-steps to ensure accuracy and stability, while retaining computational efficiency. The explicit Runge–Kutta method is preferred to a backward differentiation formula implicit solver such as DVODE [26]. An integration strategy based on the implicit solver DVODE was found to lack robustness. The implicit solver did not converge reliably near the flame-sheet, where oxidation processes drive the soot moments outside of the realizable region, thus requiring a manual resetting of the solution vector during the integration step.

## 2.2. Chemistry

The present work is based on the detailed chemical mechanism developed by Blanquart et al. [30] for the high temperature combustion of engine relevant fuels. This detailed chemical mechanism is composed of 149 species and 1651 reactions and accounts for all major pathways of PAH formation up to cyclopenta[cd]pyrene ( $C_{18}H_{10}$ ). The mechanism has been validated extensively for a large set of fuels ranging from methane to iso-octane and one-ring aromatic species using different configurations including homogeneous auto-ignition, laminar premixed flames, and laminar diffusion flames.

The rate constants of a few reactions have been updated with more recent data [31]. Among these, the reaction rate for the formation of the first aromatic ring from the recombination of an allyl and a propargyl radical



has been updated with recent quantum calculations by Miller et al. [32]. This reaction was found to be very important in correctly predicting benzene in *n*-heptane flames [30].

Before its integration in the present DNS, the original detailed mechanism was reduced to a smaller mechanism following a multi-step approach [33]. The final reduced mechanism contains only 47 species and 290 reactions and is available as [Supplemental material](#) in both CHEMKIN [34] and FlameMaster [19] formats.

### 2.2.1. Mechanism reduction

A multi-step approach combining automatic and manual reduction techniques has been used to reduce the size of the chemical mechanism and make it more affordable for DNS. Throughout the reduction process, emphasis was placed on accurately predicting the combustion characteristics of both *n*-heptane ( $C_7H_{16}$ ) and toluene ( $C_7H_8$ ), two major components typically found in surrogate fuel formulations. Ethylene was considered also as an important

target during the reduction, for most of the validation studies of soot models were performed with ethylene flames.

The first step of the reduction process relies on a manual removal of aromatic species heavier than naphthalene ( $C_{10}H_8$ ) and their corresponding chemical reactions. As described in the following sections, the inception of the first soot particles depends strongly on the concentrations of large PAH such as naphthalene, phenanthrene ( $C_{14}H_{10}$ ), and pyrene ( $C_{16}H_{10}$ ). Among these species, naphthalene plays an important role as a key intermediate in the formation of larger aromatic species. More importantly, the formation of naphthalene is believed to be the rate limiting step in the formation of large PAH [35]. In addition, naphthalene is considered to be the smallest aromatic species susceptible to forming dimers of significant lifetimes [36] and has been used often as the nucleating species [17,37]. As a result, retaining naphthalene as part of the reduced chemical model is critical. However, in order to reduce the complexity of the model, all species larger than naphthalene ( $C_{10}H_8$ ) and their corresponding chemical reactions were first removed from the detailed chemical mechanism.

Then, the resulting kinetic mechanism was reduced using the DRGEP method developed by Pepiot-Desjardins and Pitsch [33]. The automatic reduction was performed for counterflow diffusion flames of *n*-heptane/air and toluene/air in mixture fraction space at various scalar dissipation rates. The choice of configuration used for the reduction is motivated by the mode of combustion encountered in the present DNS and relevance to soot formation in general. The target species used for the reduction include the fuel, oxidizer, main combustion products ( $CO$ ,  $CO_2$ , and  $H_2O$ ), important soot precursors such as acetylene ( $C_2H_2$ ), and naphthalene. At the end of the DRGEP reduction procedure, the chemical mechanism contained 71 species and 488 reactions.

Finally, in order to reduce the size of the kinetic model further, a manual reduction was performed using appropriate species and reaction lumping, guided by a thorough reaction flux analysis. When two isomers of a species exist, such as fulvene ( $C_5H_4CH_2$ ) and benzene (cyclic  $C_6H_6$ ), these two species are combined into a single chemical species whose concentration is the sum of those of the two isomers. However, the most extensive reduction is performed with reactions lumping which consists of replacing a species by its most likely decomposition products. For instance, the butadienyl radical ( $C_4H_5$ ) is replaced by



and the phenoxy radical ( $C_6H_5O$ ) is replaced by



The final chemical mechanism obtained at the end of the multi-step reduction procedure contains 47 species and 290 reactions.

### 2.2.2. Validation cases

The reduced chemical model is validated against a series of laminar test cases, including laminar burning velocities, a rich premixed flame, and a diffusion flame. The laminar burning velocity is a fundamental and intrinsic property of a fuel and is thus a useful target for kinetic mechanism validation. In addition, a laminar premixed and diffusion flame are computed in order to analyze the capability of the reduced mechanism to predict soot precursors. Emphasis is placed on the prediction of the main products of combustion as well as on the prediction of key soot precursors such as acetylene, allene ( $CH_2CCH_2$ ), propyne ( $CH_3CCH$ ), and benzene.

First, laminar burning velocities of *n*-heptane/air mixtures are computed at various pressures and are compared to measurements [38–41]. In our computations, the laminar burning velocities were evaluated as the eigenvalue of a system of 1D ordinary differential equations describing an adiabatic unstretched premixed flat flame. As shown in Fig. 1a, the laminar flame speeds computed with the reduced chemical mechanism remain in excellent agreement with the experimental data for atmospheric pressure. Some slight differences appear for high pressure combustion (Fig. 1b). However, similar discrepancies were found in the original mechanism (not shown) and are not attributed to the reduction procedure.

Non-premixed combustion is expected to be the most dominant mode of combustion in turbulent reacting flows in which soot is formed. As a result, assessing the quality of the reduced chemical mechanism in *n*-heptane/air diffusion flames is critical. The counterflow diffusion flame by Berta et al. [42] is considered for validation, for it has been simulated already successfully with the detailed mechanism by Blanquart et al. [30]. This particular diffusion flame is characterized by a rich premixed flame on the fuel side ( $\phi = 15$ ). Figure 2 shows the mole fraction profiles for the main species and soot precursors. The decay of fuel ( $C_7H_{16}$ ) and oxidizer mole fractions is correctly represented as is the formation of the main products of combustion ( $CO$  and  $CO_2$ ). The predictions for the different soot precursors ( $C_2H_2$  and  $C_3H_4$ ) compare favorably with the experimental data with the exception of benzene, which is slightly over-predicted. However, given the large scatter between the measurements, the overall agreement with the experimental data for the benzene profile remains acceptable.

Finally, one laminar rich premixed flat flame of *n*-heptane/air ( $\phi = 1.9$ ) is considered to assess the quality of the mechanism in a rich environment. This flame, close to the sooting limit, was studied experimentally by El-Bakali et al. [43], who reported

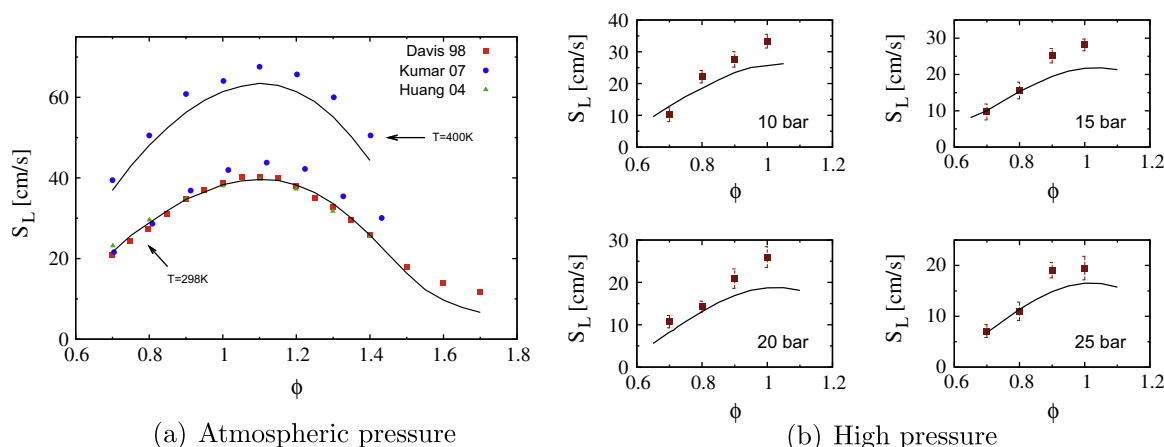


Fig. 1. Laminar burning velocities of *n*-heptane/air. References for experimental data can be found in the text.



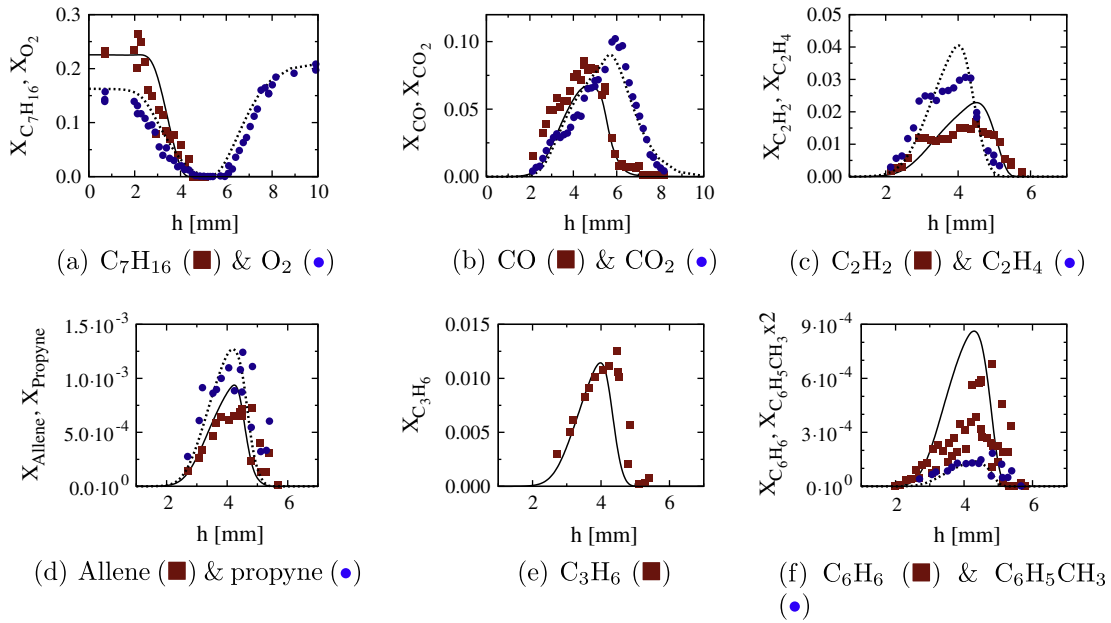


Fig. 2. Mole fractions of main species and soot precursors for the *n*-heptane diffusion flame. Experimental data from Berta et al. [42].

species concentrations and flame temperature. Because of unknown heat losses to the burner by conduction and radiation, the temperature profile was imposed in the numerical simulation. More details about the configuration may be found in Blanquart et al. [30]. As shown in Fig. 3, the decay of the fuel and the oxidizer and the formation of the main products of combustion are accurately reproduced. Furthermore, the formation of soot precursors such as acetylene, allene, propyne, and benzene also compares very well with experimental data. The over-prediction of some of the  $C_3$  species is due to the extensive reduction of the mechanism and appears to have no effect on the concentration of benzene.

### 2.3. Soot model

#### 2.3.1. Geometrical and statistical model

Soot particles and aggregates are described with two quantities: their volume ( $V$ ) and surface area ( $S$ ) [17,44]. With these two quantities, the diameter of primary particles is expressed as

$$d_p = 6VS^{-1} \quad (14)$$

and the number of primary particles per aggregate as

$$n_p = \frac{1}{36\pi} V^{-2} S^3. \quad (15)$$

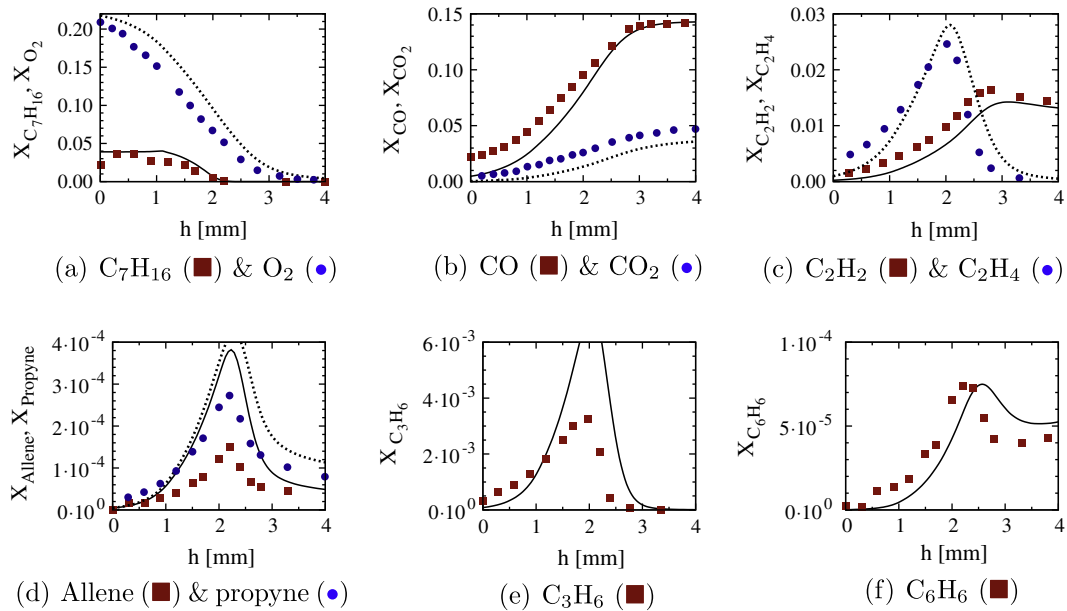


Fig. 3. Mole fractions of main species and soot precursors for the rich *n*-heptane premixed flame. Experimental data from El-Bakali et al. [43], lines are simulations.

Spherical particles are described in the limit  $n_p \rightarrow 1$ . The collision diameter of the aggregates is given by

$$d_c = d_p n_p^{1/D_f}, \quad (16)$$

where the fractal dimension  $D_f$  is taken to be 1.8, typical of soot aggregates found in flames [45].

The soot population is described statistically by a bivariate (volume and surface) number density function (NDF). Direct solution of the NDF via discretization methods is computationally intractable due to the need to describe the NDF evolution in sample space (volume and surface area) as well as physical space and time. Monte Carlo based methods are convenient and accurate in one-dimensional configurations but are not affordable in a two- or three-dimensional DNS approach. Therefore, we adopt a moment method in which equations are solved only for a few moments of the NDF. The moments of the bivariate NDF are defined as

$$M_{x,y} = \sum_i V_i^x S_i^y N_i. \quad (17)$$

Here  $M_{x,y}$  is the moment of order  $x$  for volume and  $y$  for surface, and  $V_i$ ,  $S_i$ , and  $N_i$  are the volume, surface area, and number density of a soot aggregate belonging to size class  $i$ . As for all moment methods, the rate of change of a given moment depends on additional moments, and a closure scheme is necessary.

In the present work, the Hybrid Method of Moments (HMOM) of Mueller et al. [46] is used to evaluate moments other than those solved for. The HMOM methodology can be best described as a hybrid of two other moment methods: the Method of Moments with Interpolative Closure (MOMIC) [44,47] and the Direct Quadrature Method of Moments (DQMOM) [48]. HMOM combines the interpolative closure of MOMIC with a single delta function conceptually borrowed from DQMOM. Closure is described by

$$M_{x,y} = N_0 V_0^x S_0^y + \exp \left( \sum_{r=0}^R \sum_{k=0}^r a_{r,k} x^k y^{r-k} \right) = N_0 V_0^x S_0^y + M'_{x,y}, \quad (18)$$

where  $a_{r,k}$  are the interpolation coefficients, obtained using available moments up to order  $R$ , and  $V_0$  and  $S_0$  are the volume and surface of the nucleated spherical soot particles. The first term of the equation describes the population of the smaller spherical incipient particles and models the contribution to the moments with a delta function fixed in phase space at a size corresponding to two naphthalene dimers ( $V_0 = \pi d_0^3/6$ , where  $d_0 = 0.98$  nm). The second term in Eq. (18) describes the contribution to the moments of larger soot aggregates. In this study, six statistical moments ( $R = 2$ ) are used to describe the soot population:  $M_{0,0}$ ,  $M_{0,1}$ ,  $M_{0,2}$ ,  $M_{1,0}$ ,  $M_{1,1}$ ,  $M_{2,0}$ , in addition to the weight of the delta function  $N_0$ . Eq. (8) is used to transport these quantities.

### 2.3.2. Physical processes

The soot model considers several physical and chemical processes leading to the formation (nucleation), interaction (coagulation), growth (condensation and surface growth), and destruction (oxidation) of soot particles. For more details on the physical models used in this work, the reader is referred to Blanquart and Pitsch [17]. The details of the functional form of soot source terms in the context of the HMOM closure are described by Mueller et al. [44,46].

Nucleation is the process responsible for the inception of soot particles. The model assumes nucleation occurs from the collision of two PAH dimers. A dimer is a molecular cluster composed of two PAH molecules. The rate of formation of dimers is assumed to be equal to the rate of self-collision of naphthalene molecules in the gas phase weighted by a sticking coefficient [49]. Once formed, dimers evolve according to one of two scenarios. Upon colliding with another dimer, a soot particle is formed. Alternatively, dimers can

condense on the surface of existing soot particles. Our simulation shows that as the amount of soot increases, condensation eventually surpasses nucleation as the main mode of soot mass addition due to growing surface availability for condensation.

Coagulation is the collision of two soot particles. Collision rates between soot particles are formulated to be valid from the free molecular (small collision diameter) to the continuum regime (large collision diameter). Small colliding particles are modeled as *liquid-like* [50], while colliding aggregates are modeled as rigid. When two small spherical particles collide, a larger sphere is formed. When a small spherical particle collides with a large aggregate, the small particle splashes onto the larger aggregate. Finally, when two large aggregates collide, an even larger aggregate is formed. More details about the mathematical treatment of coagulation can be found in Mueller et al. [46].

Growth by surface reactions is described by the H-abstraction/ $C_2H_2$ -addition (HACA) mechanism of Frenklach and Wang [51]. The HACA mechanism consists of a chain of elementary reactions involving hydrogen (atomic and molecular), hydroxyl radicals, water, and acetylene, leading to the addition of two carbon atoms for each completion of the reaction chain.

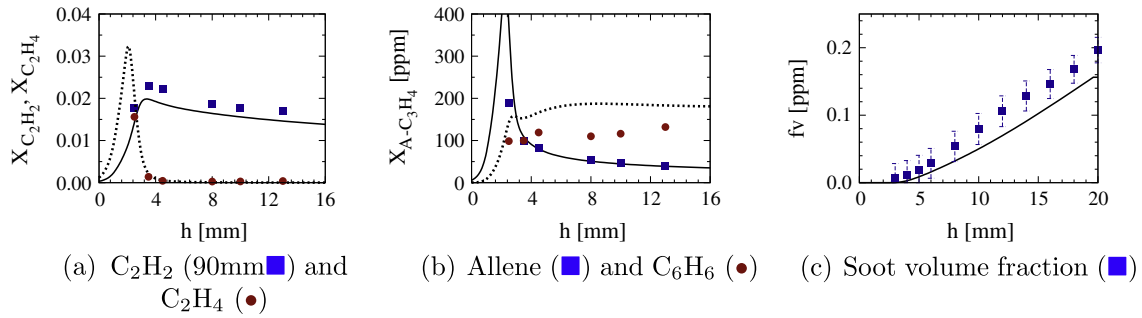
Oxidation of soot particles leads to the loss of soot mass. Despite its importance in determining soot yields in technical combustion devices (e.g. internal combustion engines), oxidation models are simplistic and largely based on semi-empirical rates inferred from laminar flame experiments [52]. Oxidation is assumed to be a function of the local concentration of OH and  $O_2$ . The resulting rates of mass loss are temperature dependent and taken from the literature. For more details on the oxidation model used, see Blanquart and Pitsch [17] and Mueller et al. [53].

### 2.3.3. Validation of soot model

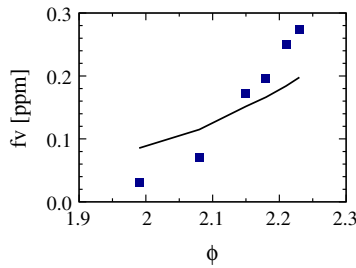
The soot model coupled with a detailed chemical mechanism has been validated in numerous numerical simulations [17,44,46,49], including high temperature premixed ethylene flames, premixed benzene flames, an acetylene counterflow diffusion flame, toluene pyrolysis in shock-tubes, and a set of premixed ethylene flames. In the present work, we validate further the soot model coupled with the reduced chemical mechanism (see Section 2.2) by simulating a series of rich premixed *n*-heptane flames [54]. These flames have equivalence ratios ranging from  $\phi = 1.99$  to  $\phi = 2.23$ .

Figure 4 compares the simulation results to experimental measurements. The concentration of various soot precursors (acetylene, ethylene, and allene) are predicted with good accuracy, with the exception of the mole fraction of benzene, which is over-predicted by 40%. As shown in Fig. 4c, the shape and magnitude of the soot volume fraction profile are well predicted. Soot particles are formed in the post flame region by nucleation and slowly grow by addition of mass through various processes including condensation and surface growth. In rich flames, the soot volume fraction keeps increasing due to an abundance of soot precursors such as acetylene and benzene.

The soot volume fraction at a given height above the burner surface ( $h = 20$  mm) is plotted in Fig. 5 as a function of equivalence ratio. The experimental data show that soot volume fraction increases as the flame becomes richer. A similar dependency of soot concentration on equivalence ratio has been observed for other fuels (acetylene, ethylene, and benzene) at various temperatures and pressures up to 100 bar [55]. As shown in Fig. 5, the detailed soot model combined with the reduced chemical mechanism is successful in reproducing the increase in soot volume fraction with equivalence ratio, albeit at a slower rate than found experimentally. These validation tests prove the ability of this modeling approach to reproduce the effects of local mixture equivalence ratio on sooting propensity.



**Fig. 4.** Mole fractions of soot precursors and soot volume fraction for the rich *n*-heptane premixed flame  $\phi = 2.18$ . Experimental data from El-Bakali et al. [54], lines are simulations.



**Fig. 5.** Evolution of soot volume fraction at  $h = 20$  mm above the burner surface as a function of equivalence ratio. Experimental data from El-Bakali et al. [54].

### 3. Initial conditions and computational parameters

The two-dimensional computational domain consists of a square of size  $L$ . Periodic boundary conditions are applied in both the horizontal ( $x$ ) and vertical ( $y$ ) directions, effectively resulting in a constant volume system. At the onset of the simulation, a horizontal strip of fuel is surrounded by oxidizer. The fuel stream consists of *n*-heptane diluted with 84.4% (by volume) nitrogen at a temperature of 300 K. The oxidizer stream consists of air (21% oxygen and 79% nitrogen) also at 300 K. The significant nitrogen dilution in the fuel stream is necessary to reduce peak soot volume fraction to a level for which radiative heat transfer from soot particles and its effect on the gas-phase can be safely neglected. The compositions of fuel and oxidizer yield a stoichiometric mixture fraction  $Z_{st} = 0.143$ . The stoichiometric scalar dissipation rate at extinction for the two streams (at 300 K and 1 atm) is  $175 \text{ s}^{-1}$ , computed in a counterflow geometry [19] employing the reduced mechanism described in Section 2.2. The background pressure, initialized at 1 atm, increases to approximately 2 atm towards the end of the simulation due to heat release. Given the modest increase in pressure during the simulation, pressure effects are not expected to play any significant role in the physical processes of interest.

Following Lignell et al. [14], the initial profile of mixture fraction in the vertical direction is given by the following equation, corresponding to a mixing layer on each side of the fuel strip

$$Z(y) = \frac{1}{4} \left( 1 + \tanh \left[ \frac{L + h_z + \delta_z - 2y}{\delta_z} \right] \right) \times \left( 1 + \tanh \left[ \frac{-L + h_z + \delta_z + 2y}{\delta_z} \right] \right), \quad (19)$$

where  $\delta_z$  is equal to the inverse of the maximum gradient of  $Z$  and controls the scalar dissipation rate at stoichiometry. The fuel strip width is indicated by  $h_z$ . The initial profile of mixture fraction is shown in Fig. 6.

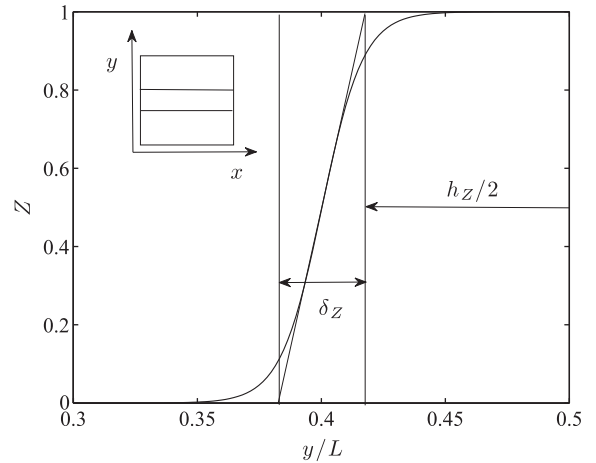


**Fig. 6.** Mixture fraction ( $Z$ ) profile along the  $y$  direction in the computational domain at the onset of the simulation. The profile is described by Eq. (19). Numerical values for the domain length  $L$ , the flame width  $h_z$  and the transition width  $\delta_z$  are shown in Table 1.

The reactive scalar fields are initialized as follows. Temperature and chemical species mass fractions are taken from a representative one-dimensional flamelet solution and mapped from mixture fraction space onto the vertical coordinate according to the mixture fraction spatial profile in Eq. (19). The one-dimensional flamelet solution is obtained at a prescribed stoichiometric scalar dissipation rate  $\chi_{st} = 60 \text{ s}^{-1}$ , corresponding to approximately one third of the extinction conditions. The scalar dissipation rate imposed to compute the one-dimensional flamelet solution matches the scalar dissipation rate in the two-dimensional computational domain along the vertical direction at the onset of the simulation. The velocity field is initialized with isotropic turbulence of prescribed fluctuations  $u'$  and integral length  $L_{11}$  according to the procedure outlined by Passot and Pouquet [56]. At the start of the simulation,  $Re_\lambda$  is equal to 170. Additionally, no soot is present in the domain at time zero.

Notwithstanding the two-dimensional treatment of turbulence, the chosen computational configuration and parameters are a reasonable approximation of the dynamics and turbulence scales characteristic of soot formation in the near field of a low Reynolds number nonpremixed turbulent jet flame.

Table 1 shows the details of all simulation parameters as well as relevant length, time, and velocity scales. The turbulence time scale  $\tau$  is defined based on  $u'$  and  $L_{11}$ , while a characteristic flame time scale is defined as  $\tau_{flame} = 2/\chi_{st}$ . The spatial resolution is sufficient to resolve the initial Kolmogorov length scale, estimated as being  $70 \text{ }\mu\text{m}$ . The fields of all species mass fractions, including radical species, are found to be well resolved throughout the

**Table 1**

Simulation parameters and relevant length, time, and velocity scales.

$L$ (mm)	60	$u'$ (cm/s)	75	$N_x \times N_y$	1200 $\times$ 1200
$L_{11}$ (mm)	4.4	$\tau$ (ms)	5.8	$\Delta x, \Delta y$ ( $\mu\text{m}$ )	50
$h_z$ (mm)	10	$\tau_{\text{flame}}$ (ms)	11.4	$\Delta t$ ( $\mu\text{s}$ )	10
$\delta_z$ (mm)	2.0	$\chi_{\text{st}}$ ( $\text{s}^{-1}$ )	60	Sim time (ms)	15

simulation. Spatial resolution requirements in a DNS of turbulent combustion are typically dictated by thin reaction fronts of radical species. Appendix B contains additional information about mesh convergence and spatial resolution considerations.

The solution is advanced up to 15 ms, which corresponds to approximately three turbulence time scales  $\tau = u'/L_{11}$  and one characteristic flame time scale. The simulation is advanced for 1500 steps with a constant time step equal to 10  $\mu\text{s}$ .

The DNS produces time dependent statistics and the simulation time may not be long enough for the velocity and scalar fields to forget the initial conditions. Despite the relatively short simulation time, the results allow drawing important and novel conclusions on the dynamics of PAH and soot particles during the early stages of soot evolution in turbulent nonpremixed flames.

Simulations were performed on Ranger, the Sun Constellation Linux Cluster at the Texas Advanced Computing Center (TACC) and on Noor, the IBM Linux Cluster at the Clean Combustion Research Center (CCRC), King Abdullah University of Science and Technology (KAUST). A typical simulation required 256 processors and took between 36 and 48 h, depending on the platform.

#### 4. Turbulent flame dynamics

Due to the strong dependence of soot growth on flame parameters such as temperature, equivalence ratio, and strain rate, turbulence/chemistry interaction is investigated first. Turbulent fluid

motion wrinkles the flame and causes the stoichiometric contour to curve and stretch throughout the domain. Instantaneous snapshots of temperature and scalar dissipation rate at times 1.5 and 10 ms are shown in Fig. 7. For the sake of clarity, only a portion of the computational domain is shown, spanning the intervals  $0.5L < x < L$  and  $0.25L < y < 0.75L$ .

Scalar dissipation rate is distributed spatially in thin, elongated layers as observed in previous experimental [57,58] and computational [59] studies. A few locations along the flame display significant weakening and extinction due to high scalar dissipation rate ( $\chi_{\text{max}} \approx 490 \text{ s}^{-1}$  at 1.5 ms). For instance, local extinction can be observed at 10 ms in the top right corner of the domain, where the stoichiometric iso-contour passes through a region of low temperatures. At locations where flame extinction occurs, the mass fraction of OH drops from its peak value of  $3.6 \times 10^{-3}$  to negligible amounts (not shown).

In the soot model used in this work, two species have significant impact on soot yield, namely naphthalene and acetylene. The concentration of naphthalene ( $\text{C}_{10}\text{H}_8$ ) governs the rates of nucleation and condensation, while the concentration of acetylene ( $\text{C}_2\text{H}_2$ ) is used in evaluating the growth rate by surface reactions. Figure 8 shows acetylene and naphthalene mass fractions at times 1.5 and 10 ms. Compared to temperature, the mass fractions of naphthalene and acetylene are affected more significantly by turbulence and by spatial and temporal variations in the scalar dissipation rate. At 10 ms, the mass fraction of naphthalene is highest in regions of low scalar dissipation rate, giving rise to concentration patches away from the flame, along the  $Z = 0.3$  iso-contour. The mass fraction of acetylene also responds to changing values of scalar dissipation rate, displaying similar spatial patterns. However, the sensitivity of acetylene to turbulent stretching appears to be less pronounced than for naphthalene.

To better analyze the effects of scalar dissipation rate on the yield of acetylene and naphthalene, the DNS results are compared

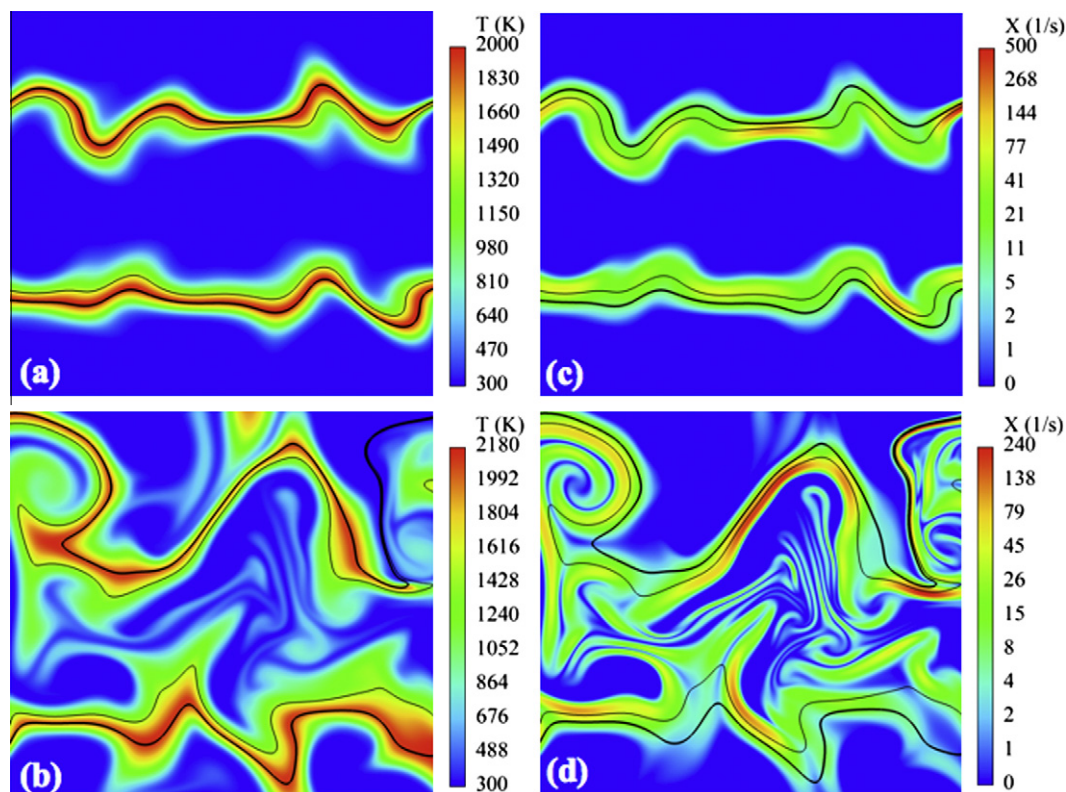


**Fig. 7.** Scalar fields of temperature (a and b) and scalar dissipation rate in logarithmic scale (c and d) at 1.5 and 10 ms (top to bottom). The thick solid black line indicates the stoichiometric iso-contour ( $Z_{\text{st}} = 0.143$ ), while the thin black line indicates the  $Z = 0.3$  iso-contour.



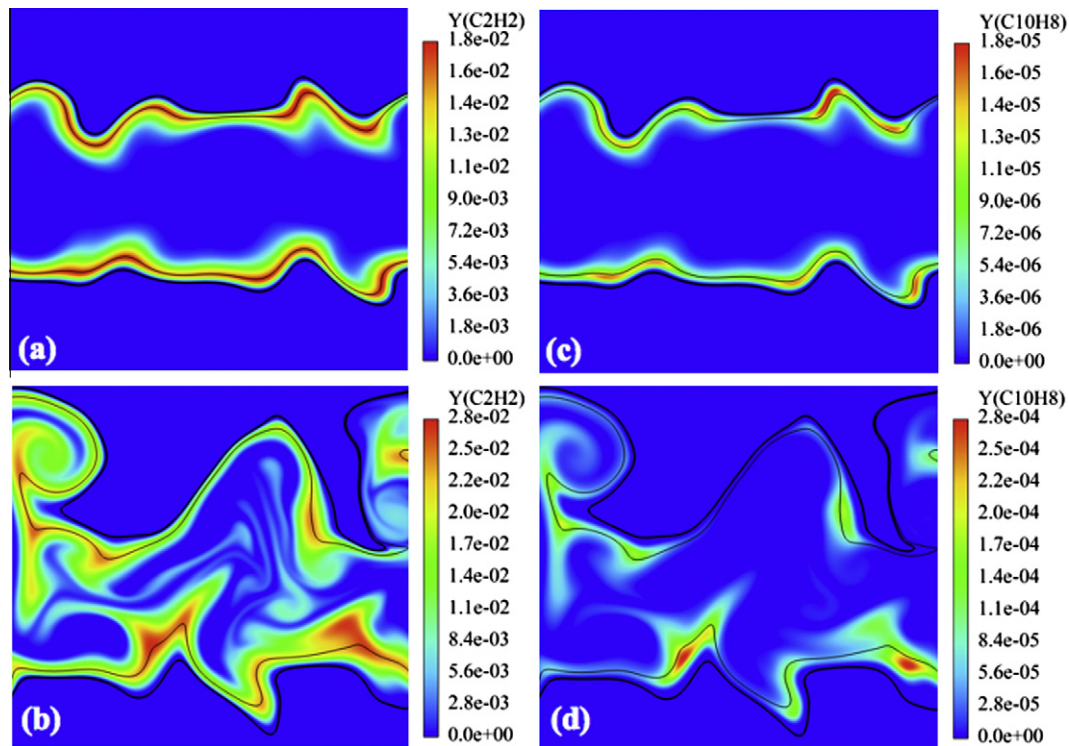


**Fig. 8.** Scalar fields of acetylene (a and b) and naphthalene mass fraction (c and d) at 1.5 and 10 ms (top to bottom). The thick solid black line indicates the stoichiometric iso-contour ( $Z_{st} = 0.143$ ), while the thin black line indicates the  $Z = 0.3$  iso-contour.

to the solutions of the steady flamelet equations [60] and are shown in Fig. 9. The data are sampled from the DNS calculation at 5 ms and along the  $Z = 0.3$  iso-contour. The  $Z = 0.3$  location was chosen as it corresponds to the peak mass fraction for both acetylene and naphthalene as found in the one-dimensional flamelet calculations. For comparison, the one-dimensional flamelet calculations were performed with the same assumptions used for the DNS (e.g. unity Lewis number, no Soret and Dufour effects, etc.) and the same reduced chemical mechanism. The background pressure is taken to be that of the DNS at 5 ms (1.19 bar).

Within the range of scalar dissipation rates encountered in the DNS, acetylene mass fraction values fall in the range  $10^{-2} < Y_{C_2H_2} < 2 \times 10^{-2}$ , while naphthalene mass fraction spans a much wider range  $10^{-6} < Y_{C_{10}H_8} < 10^{-4}$ . Even in the absence of turbulent fluctuations, the mass fraction of naphthalene displays a significantly stronger sensitivity to scalar dissipation rate compared to acetylene. With the exception of the data points at low values of scalar dissipation rates, the one-dimensional flamelet solution describes well the dependence of the mean peak mass fraction on scalar dissipation rate shown in the DNS data.

While the dependence of peak mass fraction on scalar dissipation rate observed in the DNS data is described well by the steady flamelet solution, significant scatter exists around the mean values. The magnitude of the deviation is much larger for naphthalene than for acetylene. This scatter may be explained by the rapidly changing turbulent flow field and the slowly adjusting chemical species. Furthermore, the flamelet solution at low scalar dissipation rate overestimates the mass fraction of both naphthalene and acetylene. The difference is due to unsteady flamelet effects, which are known to be more pronounced at low scalar dissipation rate [61]. The results show that naphthalene exhibits much stronger unsteady effects than acetylene, due to the slower chemistry of naphthalene (lower Damköhler number). A similar behavior is expected for PAH larger than naphthalene.

## 5. Soot dynamics and morphology

The emphasis of the present work is identifying the key mechanisms of soot growth as well as characterizing the effects of turbulent mixing on the evolution of soot. The morphology of soot particles is investigated also by focusing on aggregate properties such as the primary particle diameter and the number of primary particles.

### 5.1. Soot evolution overview

Figure 10 shows instantaneous snapshots of soot number density and soot volume fraction fields taken at 10 and 15 ms. The overall maximum values of number density and soot volume fraction are encountered at 15 ms and are  $3 \times 10^{12} \text{ cm}^{-3}$  and 0.21 ppm, respectively. As seen in Fig. 10, the spatial distribution of soot exhibits two distinct patterns: (a) small islands/patches of large values of soot number density and volume fraction; and (b) sharp fronts and filament-like patterns. While the islands appear to accumulate preferentially along the  $Z = 0.3$  iso-contour, the filaments penetrate deep into the fuel stream, marking the edges of eddies. The number and length of the filaments increase with time as turbulent eddies stretch soot patches across the domain [14] in the absence of diffusive transport. Due to the high Schmidt number (or low mass diffusivity) typical of soot transport, soot particles do not diffuse, and their transport is controlled mostly by convection and to a much lesser extent by thermophoresis.

Soot begins nucleating on the rich side of the flame sheet at a location where naphthalene abounds ( $Z \approx 0.3$ ). From the onset of the simulation and up to 5 ms, the rate of increase of soot mass is dominated by the nucleation of spherical soot particles. At early times, soot consists of a large number of small, spherical particles, and the soot particle size distribution is monodisperse. The mean

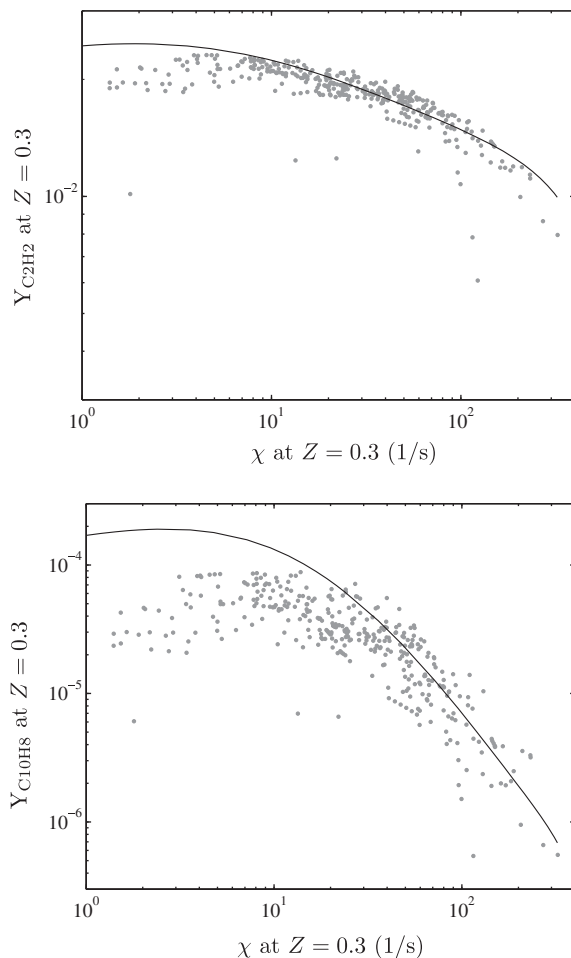


**Fig. 9.** Mass fraction of acetylene and naphthalene as a function of scalar dissipation rate. Samples taken at  $Z = 0.3$ . DNS data sampled at 5 ms. Acetylene,  $C_2H_2$  (top); naphthalene,  $C_{10}H_8$  (bottom): — steady flamelet solution [19]; ·, DNS data.

diameter and number of primary particles at 1.5 ms are spatially homogeneous and equal to 0.98 nm and 1, respectively (not shown). Meanwhile, naphthalene dimers condense on the surface of existing particles. During the simulation, the overall rate of condensation increases as existing particles grow and more surface becomes available. At 10 ms, condensation emerges as the physical process contributing most to soot mass growth. Intense growth occurs in regions of high concentration of naphthalene and low scalar dissipation rate as is evident by comparing visually Fig. 8d and Fig. 10c. For instance, at 10 ms, a patch of naphthalene mass fraction appears near the bottom left corner of Fig. 8d where there is a peak in soot volume fraction (see Fig. 10c). The patch-like soot patterns observed in the domain are identified as regions of naphthalene-based soot growth at locations of low scalar dissipation rate.

The patch-like structure of soot and PAH provides insight into the process physics and its modeling. From a physical perspective, the sensitivity of PAH species to hydrodynamic strain and unsteady scalar dissipation rate indicates that turbulent mixing in technical combustion devices can lead to soot growth suppression, while having limited effect on the fuel oxidation chemistry. Based on the results presented, the dependence of soot yield on the mixing rate can be explained by the sensitivity of PAH to scalar dissipation rate. Hydrodynamic strain effects are expected to be particularly important for nonpremixed and low-temperature premixed flames. A lesser sensitivity of soot growth rates to strain is expected for high-temperature premixed flames due to surface

reactions being the dominant growth process. Surface growth rates depend on the concentration of acetylene, which is less sensitive to strain. From a modeling perspective, soot growth models that rely on smaller hydrocarbon species as a proxy for large PAH molecules ignore or misrepresent the effects of turbulent mixing and hydrodynamic strain on soot formation due to differences between the Damköhler number of small and large hydrocarbon species. For example, acetylene is often used as an indicative critical species in the soot formation process [13] in order to simplify the treatment of gas phase chemistry. As shown in this work, the sensitivity of acetylene to turbulent mixing is significantly less pronounced than naphthalene. Therefore, the application of a soot model relying on acetylene-based mass growth to a configuration for which PAH-based growth is the dominant growth route will misrepresent the effect of hydrodynamic strain on the overall soot yield.

Instantaneous snapshots of the mean primary particle diameter and mean number of primary particles per aggregate are shown in Fig. 11. These two quantities describe the morphology of soot particles. The overall maximum values of primary particle diameter and number of primary particles per aggregate are encountered at 15 ms with values around 2.9 nm and 1000, respectively. A visual comparison between Fig. 10d (soot volume fraction) and Fig. 11b (primary particle diameter) reveals that the regions populated by aggregates with the largest primary particles are also characterized by the highest soot volume fraction. This is evident in the case of a soot pocket located at the bottom of the domain where the mean primary particle diameter is 2.9 nm and soot volume fraction is 0.21 ppm. In regions where nucleation is persistent, such as along the  $Z = 0.3$  iso-contour, the mean number of primary particles per aggregate is maintained low by the continuous addition of new spherical particles. When streaks of soot are convected away from regions of intense nucleation, the nucleation rate decreases, while frequent collisions quickly lower the number density and increase the number of primary particles per aggregate. Figure 11d shows a long soot streak stretching into the fuel stream at 15 ms. Along the soot filament, the mean number of primary particles per aggregate exceeds 1000, and the number density is the lowest in the domain (see Fig. 10b).

## 5.2. Soot transport and growth processes

Soot growth and oxidation rates are a function of temperature and mixture composition. While local mixture fraction determines nucleation, condensation, and oxidation rates, it provides limited information about quantities such as soot number density and volume fraction. This is due to soot experiencing significant motion in mixture fraction space because of differential diffusion effects among soot and gas-phase species. Differential diffusion effects are important in soot transport and were first discussed and analyzed by Pitsch et al. [62]. In a simple candle flame, differential diffusion causes soot to be transported towards the flame sheet where it is oxidized. This process is similarly responsible for soot burnout in diesel engines and aircraft engine combustors.

A convenient description of the motion of a mixture fraction ( $Z$ ) iso-surface relative to fluid convection is provided by the iso-surface displacement velocity [63]

$$\mathbf{v}_Z = v_Z \mathbf{n} = - \frac{\nabla \cdot (\rho D_{th} \nabla Z)}{\rho |\nabla Z|} \mathbf{n}, \quad (20)$$

where  $\mathbf{n}$  indicates the vector normal to the surface defined as  $\mathbf{n} = \nabla Z / |\nabla Z|$ . The mixture fraction mass diffusivity is set equal to the thermal diffusivity  $D_{th}$ . The scalar quantity  $v_Z$  is called the iso-surface displacement speed and takes both positive and negative values. Due to negligible mass diffusivity [20], soot particles are convected with the flow, and the displacement speed describes

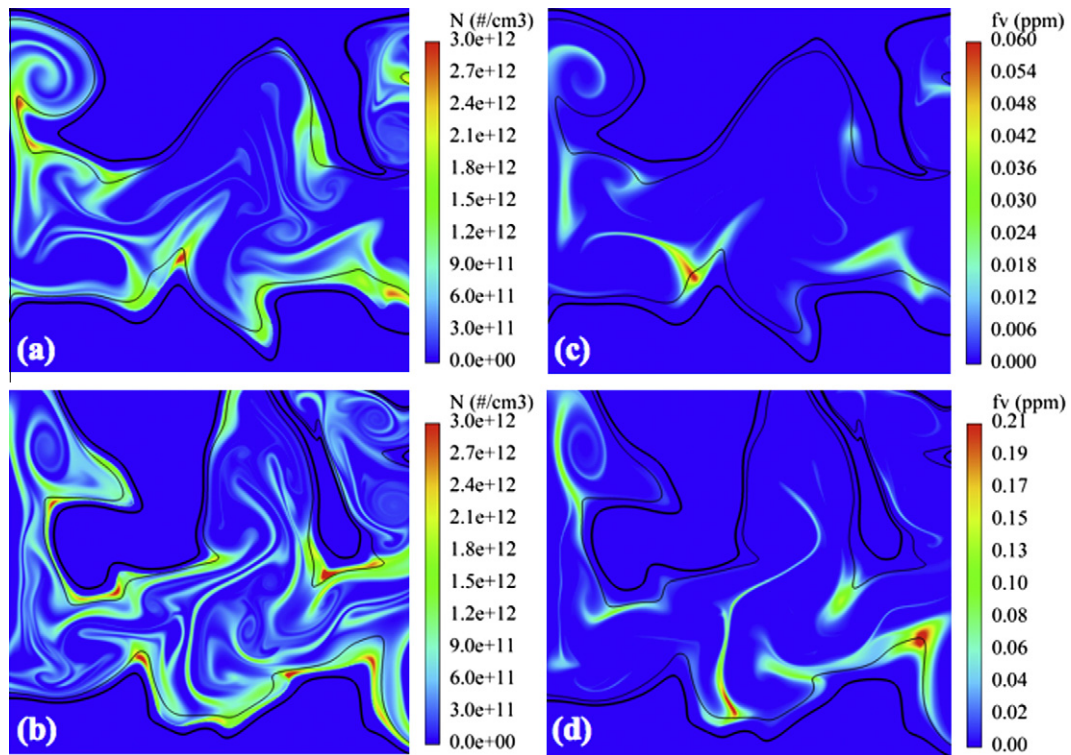


**Fig. 10.** Scalar fields of soot particle number density,  $N$  (a and b) and soot volume fraction,  $f_v$  (c and d) at 10 (top) and 15 ms (bottom). The thick solid black line indicates the stoichiometric iso-contour ( $Z_{st} = 0.143$ ), while the thin black line indicates the  $Z = 0.3$  iso-contour.

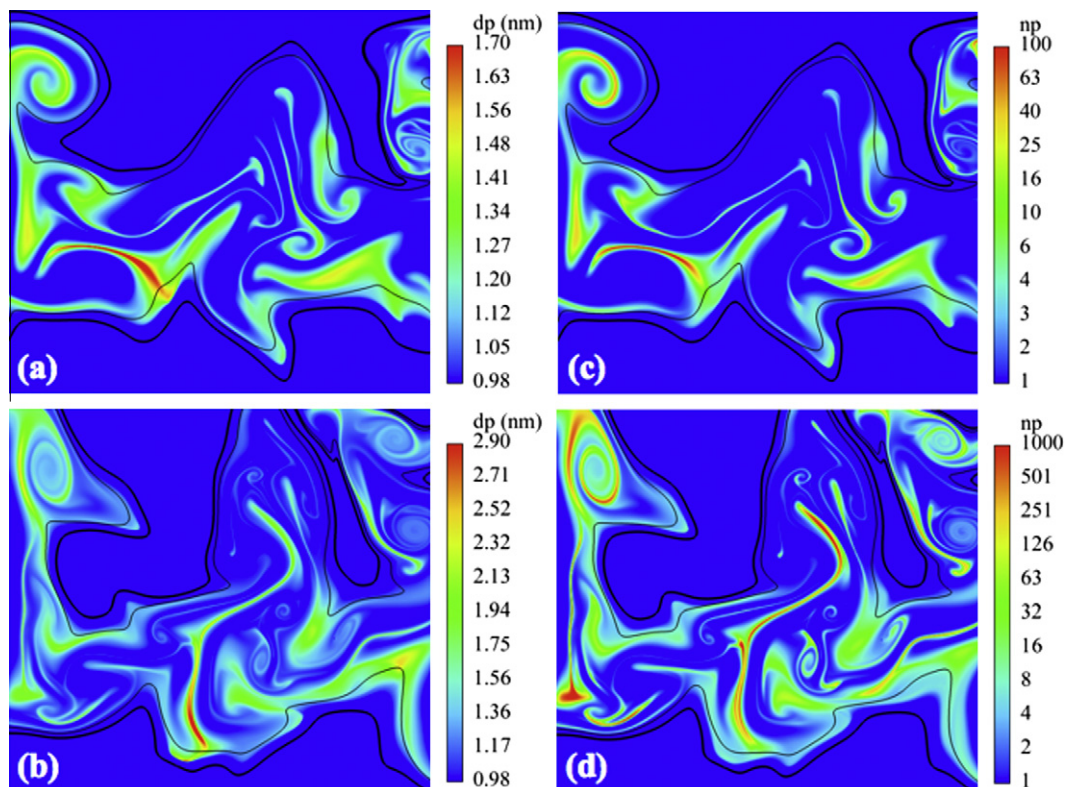


**Fig. 11.** Scalar field of soot primary particle diameter,  $d_p$  (a and b), and number of primary particles per aggregate,  $n_p$ , in logarithmic scale (c and d) at times 10 ms (top) and 15 ms (bottom). The thick solid black line indicates the stoichiometric iso-contour ( $Z_{st} = 0.143$ ), while the thin black line indicates the  $Z = 0.3$  iso-contour.



the movement of soot relative to a given mixture fraction iso-contour. Thermophoresis contributes to the movement of soot in mixture fraction space also. However, for the conditions of the present DNS, we find that thermophoretic velocities normal to the  $Z = 0.3$  iso-contour remain well below 3 cm/s and are thus neglected.

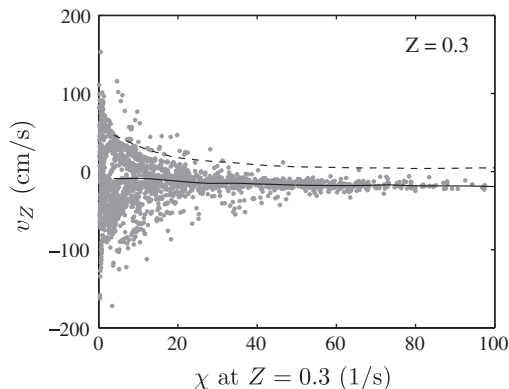
Lignell et al. [14,15] adopted the displacement speed formalism to describe quantitatively the differential diffusion process between soot and gas-phase in a DNS of turbulent combustion. The same approach is used in this work. The results obtained in the present study confirm the statistics of the displacement speed previously described by Lignell et al. [14,15]. However, differently from their work, the iso-contour of interest lies away from the reaction zone of the flame at a location where soot growth processes are dominated by PAH-based growth. As will be shown, the implications of particle differential transport on soot growth are very different between the present and previous work [14,15].

Figure 12 shows the displacement speed  $v_Z$  versus scalar dissipation rate  $\chi_Z$  along the  $Z = 0.3$  iso-contour. The data are sampled at the end of the simulation (15 ms). The  $Z = 0.3$  iso-contour is preferred to the stoichiometric contour adopted in other studies on sooting flames [9,14,15] because it corresponds approximately to the location of peak soot growth rates and soot volume fraction for the chosen stream compositions. Two distinct regimes can be identified. At locations of low scalar dissipation rate, the absolute value of the displacement speed is largest, and  $v_Z$  displays both negative and positive values. On the contrary, in regions of high scalar dissipation rate, the displacement speed is lowest and mostly negative. The mean displacement speed conditioned on scalar dissipation rate is constant across the range of scalar dissipation rates observed. The conditional mean displays a minor negative bias as reported in previous studies on turbulent flames [14,64] in configurations similar to the one investigated in this work. For longer simulation times and overall lean conditions, the mean displacement speed increases with time eventually becoming positive [15]. Mixing reduces the peak mixture fraction value and the fraction of positive displacement speed increases as soot is convected towards the flame sheet.

In order to better understand the spatial distribution of the displacement speed, the expression for  $v_Z$  in Eq. (20) is written as the sum of two terms [65]:

$$v_Z = -D_{th} \nabla \cdot \mathbf{n} - \frac{1}{\rho |\nabla Z|} \frac{\partial}{\partial \eta} \left( \rho D_{th} \frac{\partial Z}{\partial \eta} \right), \quad (21)$$

where  $\eta$  indicates the normal coordinate across the iso-contour directed towards increasing values of  $Z$ . The first term is proportional to the iso-contour curvature (curvature term) and the second term



**Fig. 12.** Conditional statistics of the displacement speed  $v_Z$  as in Eq. (20) along the  $Z = 0.3$  iso-contour versus the local scalar dissipation rate at 15 ms. —, mean; ---, standard deviation; ·, data.

is proportional to the spatial derivative of the mixture fraction gradient along the normal (normal term). By definition of the normal vector, the curvature is positive when the center of curvature lies on the lean side of the iso-contour. For a flat, nonpremixed flame, the expression for the displacement speed reduces to the normal term and  $v_Z(\hat{Z}) < 0$  for  $\hat{Z} \lesssim 0.5$ . The opposite occurs for  $\hat{Z} \gtrsim 0.5$ .

Figure 13 illustrates the contribution of the two terms in Eq. (21) to the overall displacement speed. The data are binned with respect to the resulting displacement speed to highlight the relative importance of the two terms for a given value of  $v_Z$ . Except in the case of very small values of the displacement speed, the curvature and normal terms have the same sign and act synergistically. This fact allows to judge the sign of the displacement speed from the sign of the curvature or normal component alone. Also, the mean values of the two components are similar, indicating that (on average) they contribute equally to the resulting displacement speed. Finally, at locations where the curvature term is the largest in the domain, the normal term is negligible. Hence, at locations of maximum iso-contour curvature, the displacement speed is solely due to the curvature component.

Based 1–3 on the data presented, we conclude that soot particles in regions of positive iso-contour curvature (center of curvature on the lean side of the iso-contour) move towards richer mixtures (negative displacement speed); the opposite occurs for soot particles in regions of negative curvature and positive displacement speed.

An important connection between soot volume fraction and iso-contour curvature is established by the correlation between curvature and scalar dissipation rate along the  $Z = 0.3$  iso-contour. The data are shown in Fig. 14 where a negative correlation between curvature and scalar dissipation rate is apparent: regions of high curvature are characterized by low scalar dissipation rate. Due to the sensitivity of PAH to scalar dissipation rate, regions of high curvature are characterized by sustained soot nucleation and growth and (eventually) the highest soot volume fraction (see Fig. 15). The mean soot volume fraction along three iso-contours around the location of peak growth ( $Z = \{0.23, 0.26, 0.3, 0.34\}$ ) increases for increasing absolute value of the curvature, reaching a minimum at zero curvature. The mean soot volume fraction profiles are approximately symmetric for positive and negative curvatures. A small, but obvious bias in favor of positive curvature and negative displacement speed appears as the data are sampled along increasingly rich iso-contours.

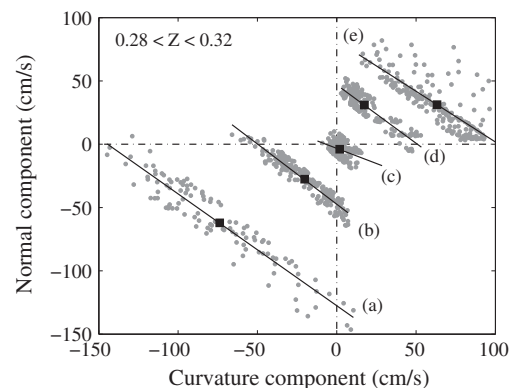


**Fig. 13.** Statistics of the curvature and normal components of the displacement velocity  $v_Z$ , the first and second term in Eq. (21), respectively. The data are sampled along mixture fraction iso-contours  $0.28 < Z < 0.32$  at 15 ms. The solid lines are linear least square fits to five sets of data, binned according to the value of the displacement velocity: (a)  $-160 < v_Z < -140$ , (b)  $-60 < v_Z < -40$ , (c)  $-10 < v_Z < 10$ , (d)  $40 < v_Z < 60$ , (e)  $80 < v_Z < 100$  (cm/s). For each set, the mean values of the two displacement velocity components is indicated by a solid square.



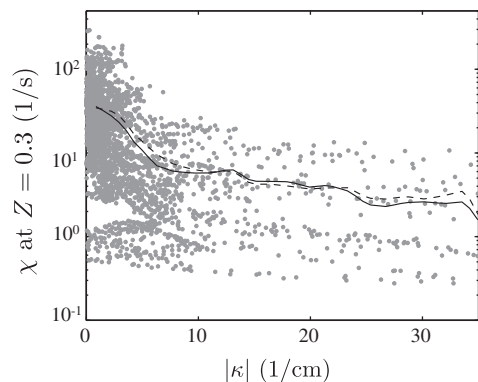


**Fig. 14.** Statistics of scalar dissipation rate conditioned on the absolute value of the iso-contour curvature ( $|\kappa| = |\nabla \cdot \mathbf{n}|$ ) at 15 ms. —, mean; - - -, standard deviation; ·, data. The data are sampled along the  $Z = 0.3$  iso-contour.

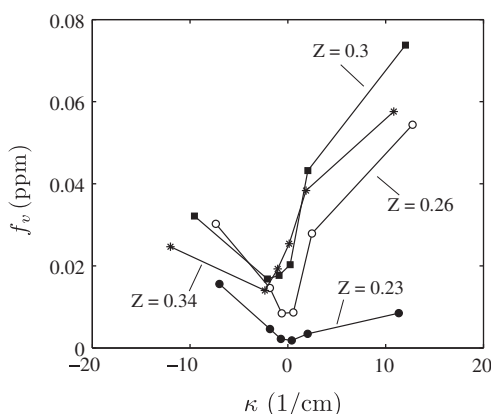


**Fig. 15.** Mean soot volume fraction along four mixture fraction iso-contours ( $Z = \{0.23, 0.26, 0.3, 0.34\}$ ) conditioned on the local value of the iso-contour curvature ( $\kappa = \nabla \cdot \mathbf{n}$ ). Data sampled at 15 ms.

Due to the symmetry in the statistics of the displacement speed at low scalar dissipation rate, movement towards leaner or richer compositions is almost equally likely. The displacement direction established by the sign of the iso-contour curvature determines the subsequent soot evolution. Soot moving towards the flame (negative curvature) first grows by surface reaction via the HACA mechanism at locations of high temperature and acetylene concentration. As the displacement continues, soot is oxidized near the flame sheet. The occurrence of surface growth followed by oxidation at the flame sheet was first described by Pitsch et al. [62] in the context of unsteady flamelets and recently demonstrated in two DNS studies of turbulent sooting flames [14,15].

To summarize, regions of high curvature are regions of low scalar dissipation rate as shown in Fig. 14. Regions of low scalar dissipation rate (and high curvature) are regions of large displacement speed (see Fig. 12). At locations of low scalar dissipation rate (and high curvature), high PAH concentration are present (see Figs. 9 and 15).

Due to the inverse correlation between curvature and scalar dissipation rate, the most rapid displacement in mixture fraction space occurs at locations where abundant PAH species generate the highest values of soot volume fraction. The correlation between high values of soot growth rates and pronounced differential diffusion motion in  $Z$ -space explains the observed soot distribution and growth patterns in mixture fraction space. First, soot nucleates around  $Z = 0.26$  in regions of low scalar dissipation rate. Soot particles in those regions characterized by positive curvature are

displaced towards richer mixtures. During this relative motion, mass growth continues sustained by PAH species condensation on soot particles. Growth by condensation eventually surpasses growth by nucleation as more soot surface becomes available. Since the concentration of naphthalene decreases monotonically for  $Z > 0.26$ , soot growth rates decrease as the aggregates are displaced further towards richer mixtures and cross the  $Z = 0.3$  iso-contour. Soot volume fraction peaks approximately at  $Z = 0.31$ , i.e. at richer conditions than those of peak nucleation and peak condensation due to a drift in mixture fraction space caused by differential diffusion. On average, soot growth due to surface reactions is maximum at  $Z = 0.23$ , i.e. at mixture compositions leaner than those characteristic of peak nucleation. The location of peak soot volume fraction and peak soot growth rates in mixture fraction space during the simulation are shown in Fig. 16. It is also observed that the locations of peak growth due to nucleation, condensation and surface reactions remain approximately constant throughout the simulation.

Despite the movement of soot in mixture fraction space being nearly symmetric, the spatial distribution of soot volume fraction is significantly biased towards the fuel stream due to higher PAH-based growth rates at rich mixtures and an oxidizing environment next to the flame sheet.

### 5.3. Statistical analysis of soot dynamics

Figures 17 and 18 show the soot number density and volume fraction conditioned on mixture fraction at different times in the simulation. Nucleation generates numerous monodisperse spherical soot particles at the onset of the simulation (1.5 ms). The monodisperse nature of the nucleated particles is reflected in the linear correlation between soot number density (Fig. 17a) and volume fraction (Fig. 18a). The most intense nucleation occurs at  $Z \approx 0.3$ . At richer mixture fractions, nucleation rates decrease due to diminishing PAH concentration.

Figures 17b and 18b illustrate that, by the end of the simulation (15 ms), differential diffusion has spread soot throughout the entire mixture fraction space. In contrast to the initial stages, soot quantities (e.g. number density and volume fraction) and mixture fraction are significantly less correlated. In addition, soot number density and volume fraction are also no longer correlated to one another. Soot volume fraction is maximum around  $Z = 0.3$  and declines slowly as the mixture becomes richer. At leaner mixtures, soot volume fraction and number density decline rapidly near  $Z = 0.2$  due to intense oxidation next to the flame sheet. Figure 17b shows that soot particles accumulate preferentially in the fuel

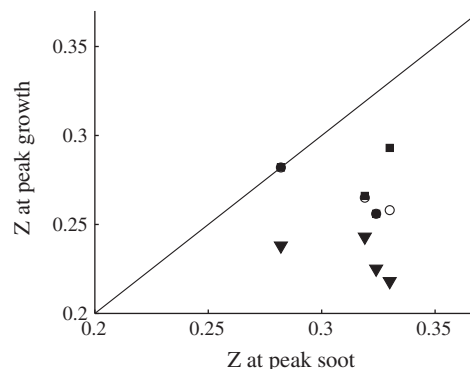


**Fig. 16.** Mixture fractions at peak soot volume fraction and peak soot growth rate. Growth due to nucleation (open circles), condensation (solid squares) and surface reactions (solid triangles) is shown. The data are taken from the domain at 1.5, 5, 10 and 15 ms. On average, nucleation peaks at  $Z = 0.26$ , condensation at  $Z = 0.27$ , and surface growth at  $Z = 0.23$ , while soot accumulates at  $Z = 0.31$ .

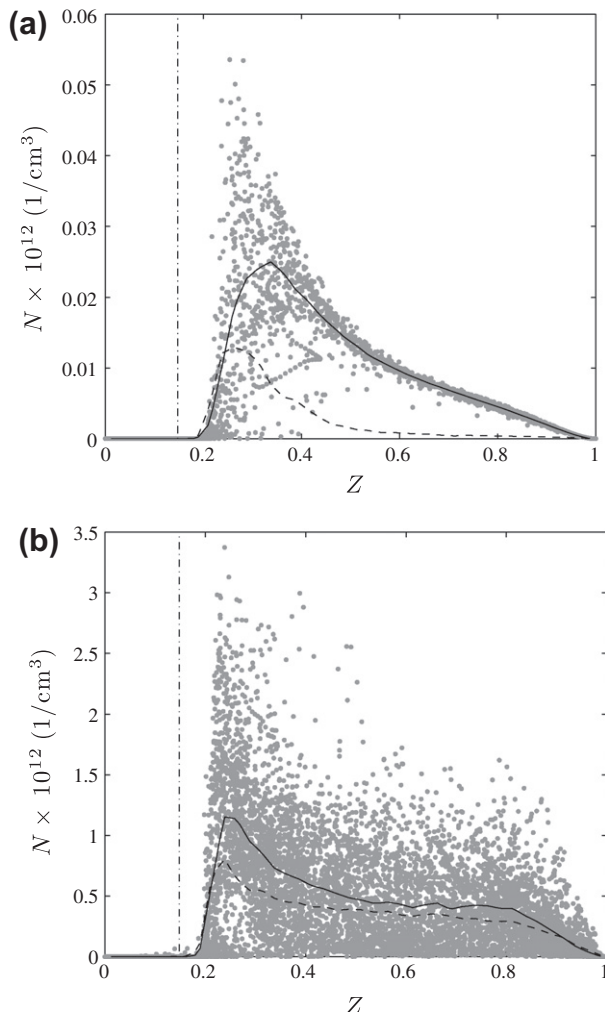


**Fig. 17.** Statistics of soot number density ( $N$ ) conditioned on local mixture fraction ( $Z$ ). (a)  $t = 1.5$  ms, (b)  $t = 15$  ms. —, mean; - - -, standard deviation; ·, data. The vertical dashed-dotted line indicates the location of stoichiometric mixture fraction ( $Z_{st} = 0.143$ ).

stream. This observation holds in the early stages of the evolution of soot. As previously discussed, at a later stage soot will move towards the flame sheet due to differential diffusion.

The conditional mean and standard deviation of soot quantities have similar magnitude. At times, the standard deviation may even exceed the mean value. High values of variance reflect the *intermittent* presence of soot along mixture fraction iso-contours. The spatially intermittent distribution of soot is also apparent in Fig. 10 and is due to differential diffusion and scalar dissipation rate effects as discussed previously (see Section 5.2).

The growth rate of soot volume fraction due to nucleation, condensation, and surface reaction and the rate of mass loss due to oxidation are averaged along mixture fraction iso-contours and shown in Fig. 19. Nucleation and condensation contribute the most to soot growth at both 5 and 15 ms. Combined, they surpass surface growth by a factor of five and ten at 5 and 15 ms, respectively. By 15 ms, as more surface becomes available, the contribution of condensation has surpassed that of nucleation, which dominates at the onset of the simulation (5 ms). The two contributions are found equal at 10 ms (not shown). Nucleation and condensation processes dominate over surface reactions in determining soot growth rates in nonpremixed turbulent flames.

Interestingly, oxidation rates peak at  $Z = 0.22$  near the flame sheet where growth due to surface reactions is also maximum.

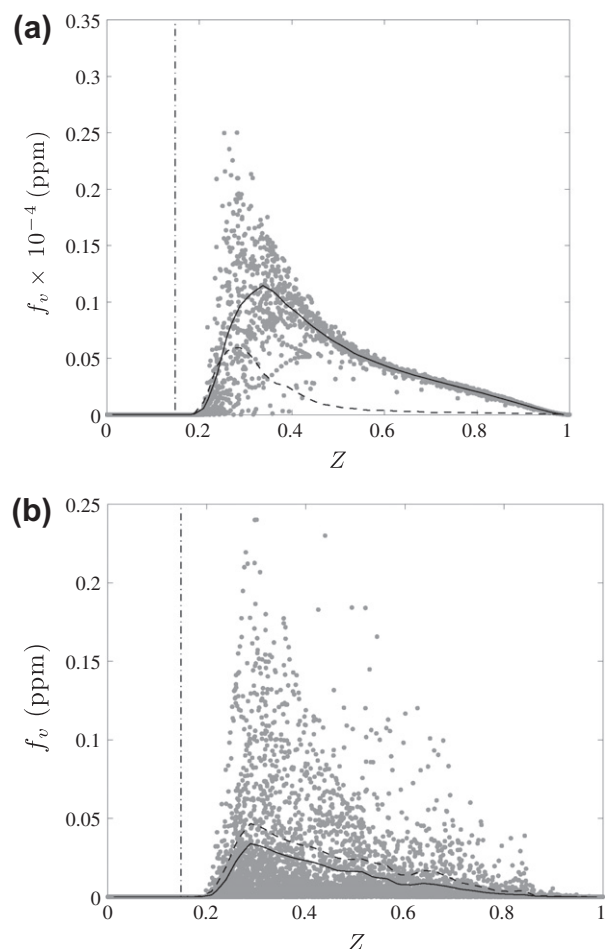


**Fig. 18.** Statistics of soot volume fraction ( $f_v$ ) conditioned on local mixture fraction ( $Z$ ). (a)  $t = 1.5$  ms, (b)  $t = 15$  ms. —, mean; - - -, standard deviation; ·, data. The vertical dashed-dotted line indicates the location of stoichiometric mixture fraction ( $Z_{st} = 0.143$ ).

The rate of oxidation per unit soot surface area is maximum at the flame sheet ( $Z_{st} = 0.143$ ) due to high temperature and the abundance of hydroxyl radical and molecular oxygen species. As soot is displaced towards the flame sheet and oxidized, the reduction of surface available for oxidation slows down the overall rate of mass loss. As a result, the maximum oxidation rate is established at a distance from the flame and not at stoichiometric conditions.

#### 5.4. Statistical analysis of the morphology of soot particles

Data on the mean diameter and number of primary particles per aggregate at 15 ms are shown in Fig. 20. Recall that nucleated soot particles are spheres of identical diameter equal to 0.98 nm. The mean primary particle diameter reaches a maximum of 1.5 nm near  $Z \approx 0.4$  and decreases slowly as mixture fraction increases. The largest primary particles populate the location of peak concentration of PAH and peak soot, suggesting that primary particle diameter growth is due to condensation and collisions of the small, incipient particles with large mature aggregates. Primary particles with diameters as large as 3 nm exist around  $Z = 0.5$  but are considerably less numerous.

The conditional mean of the number of primary particles per aggregate increases monotonically with mixture fraction up to  $Z = 0.7$ , where a maximum is reached. By 15 ms, aggregates have up to 100 primary particles on average. Aggregates with as many as  $3 \times 10^3$  primary particles exist in the domain. The location of

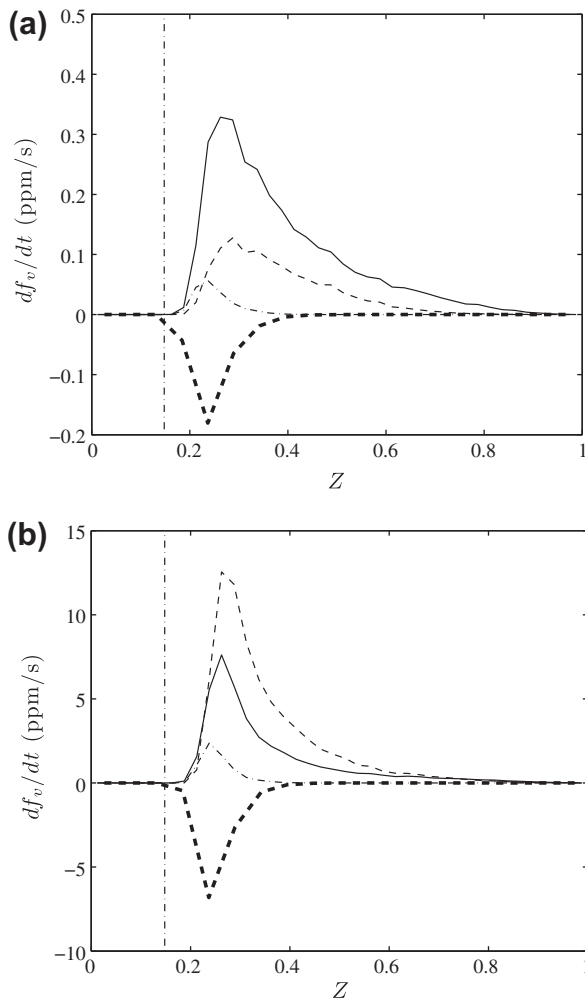


**Fig. 19.** Statistics of soot growth and oxidation rates conditioned on local mixture fraction ( $Z$ ). (a)  $t = 5$  ms, (b)  $t = 15$  ms. —, nucleation; ---, condensation; - · - ·, surface reaction; · · · ·, oxidation. The vertical dashed-dotted line indicates the location of stoichiometric mixture fraction ( $Z_{st} = 0.143$ ).

the maximum ( $Z = 0.7$ ) is removed from the location of peak nucleation at  $Z \approx 0.26$  since differential diffusion induces a significant drift of soot in mixture fraction space towards increasing  $Z$ . As aggregates are convected towards richer mixtures, collisions promote an increase in the number of primary particles per aggregate while nucleation and condensation rates are reduced due to diminished PAH concentrations.

The joint statistics of size and number of primary particles in soot aggregates are shown in Fig. 21 to further illustrate the morphological characteristics of soot. Aggregates accounting for the most soot volume fraction are characterized by the largest primary particles and an intermediate number of primary particles ( $\approx 80$ ). The aggregates with the most primary particles ( $\approx 120$ ) are responsible for less soot mass. Those findings confirm that some aggregates are rapidly displaced at compositions much richer than those in regions of peak growth. The growth of primary particles is interrupted by a swift displacement towards richer compositions, while collisions result in a large number of particles per aggregate.

The aggregate properties presented thus far contain contributions from both the smaller spherical particles and the larger aggregates. The ratio of the number density of the smaller spherical particles to the total number density is shown in Fig. 22. Near the location of peak nucleation ( $Z = 0.26$ ), much of the soot population

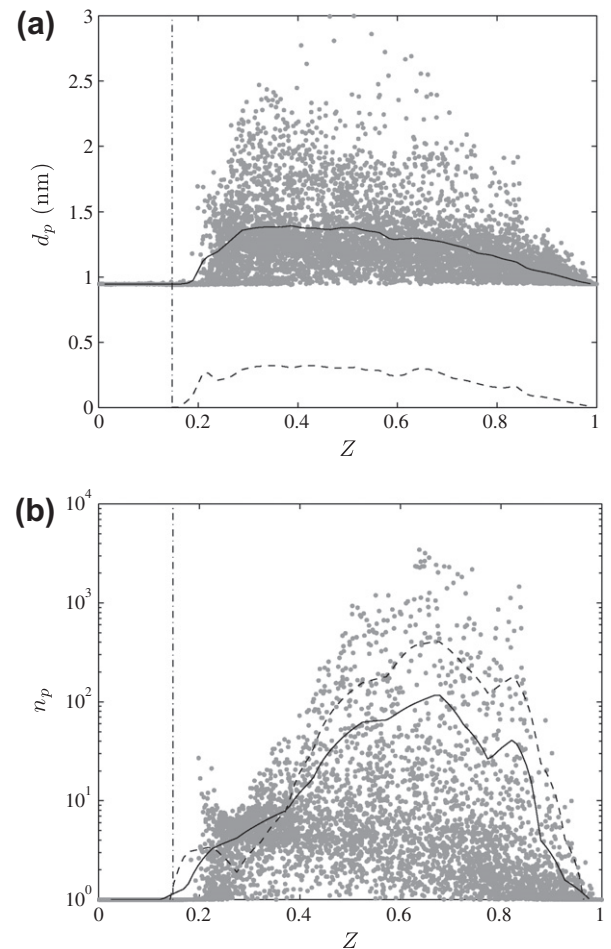


**Fig. 20.** Statistics of diameter ( $d_p$ ) and number ( $n_p$ ) of primary particles per aggregate conditioned on local mixture fraction ( $Z$ ) at 15 ms. (a)  $d_p$  (nm); (b)  $n_p$  (logarithmic scale). —, mean; ---, standard deviation; ·, data. The vertical dashed-dotted line indicates the location of stoichiometric mixture fraction ( $Z_{st} = 0.143$ ).

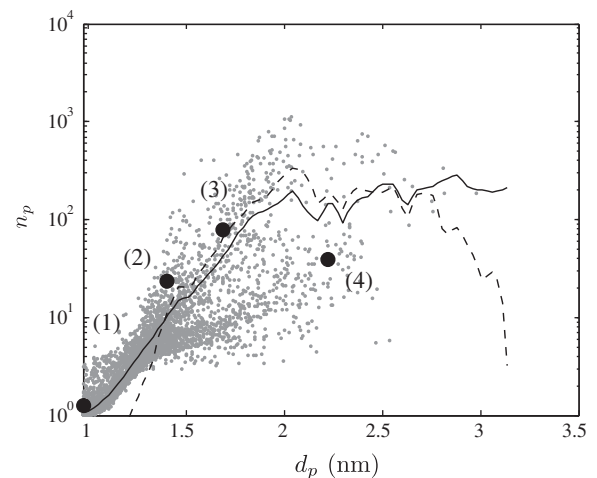


**Fig. 21.** Statistics of the number ( $n_p$ ) of primary particles per aggregate conditioned on the value of the primary particle diameter ( $d_p$ ) at 15 ms. —, mean; ---, standard deviation; ·, data. The solid circles and labels indicate mean values conditioned on increasing soot volume fraction (from 1 to 4).

is smaller spheres. However, as the mixture fraction increases, very few of the smaller particles remain. The reduction is due to two

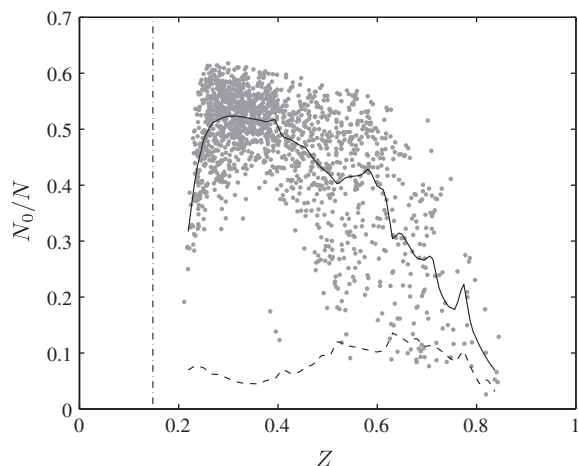


**Fig. 22.** Statistics of the ratio between the number of small particles and the total number of soot particles ( $N_0/N$ ) conditioned on the local mixture fraction at 15 ms. —, mean; ---, standard deviation; ·, data. The vertical dashed-dotted line indicates the location of stoichiometric mixture fraction ( $Z_{st} = 0.143$ ). Statistics are computed based on samples having a soot volume fraction greater than 1% of the maximum soot volume fraction (0.5 ppm).

reasons. First, at very rich mixture fractions, PAH concentrations are reduced, so nucleation, the source of the small particles, ceases. Second, the smaller particles collide with one another and the larger aggregates present to form even larger particles.

These observations complete the analysis of the evolution of the soot population described in the previous sections. Soot moving

towards rich mixtures is first monodisperse as nucleation is the sole active process near  $Z = 0.26$ . Once sufficient surface area is available, condensation surpasses nucleation as the dominant growth mechanism. Coagulation is active simultaneously with condensation, resulting in an increase in the average number of primary particles per aggregate and a decrease in the number density. At even richer mixtures, nucleation and condensation cease, leaving coagulation as the only active process. At these compositions, the population consists of primarily large aggregates with virtually no smaller spherical particles.

## 6. Concluding remarks

This study investigates the formation and early evolution of soot in a turbulent nonpremixed flame subject to isotropic decaying turbulence.

For the first time, a DNS of a turbulent sooting flame includes finite rate chemistry of Polycyclic Aromatic Hydrocarbons (PAH), which are widely accepted as being precursors to soot particles. The recently developed HMOM soot model [46] is adopted to represent statistically soot number density, volume fraction, and morphological attributes of aggregates, such as size and number of primary particles per aggregate. Compared to widely used, semi-empirical soot models [11,13], HMOM describes the effect of persistent nucleation on the statistics of soot, effectively allowing for an accurate description of both number density and volume fraction.

Our DNS results show that soot nucleates on the rich side of the flame in regions of high PAH concentration. Particle nucleation

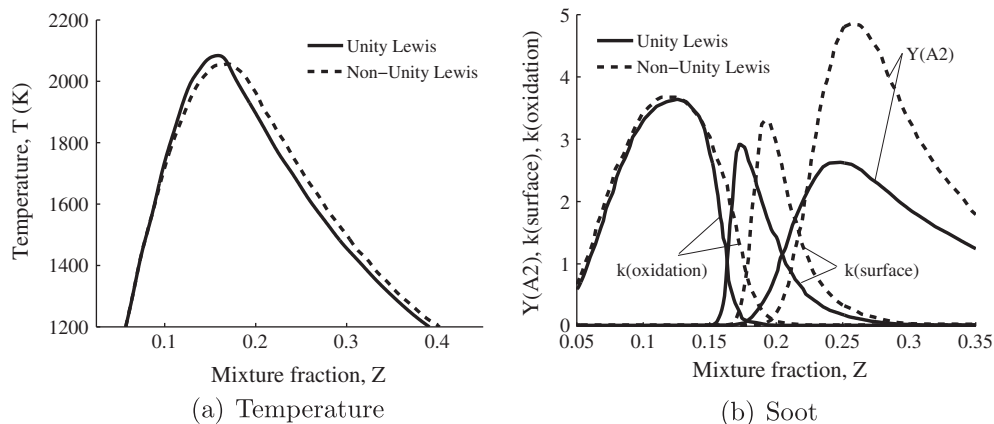


**Fig. 23.** Solutions to the steady flamelet equations for unity (solid) and non-unity (dashed) Lewis number. The flamelet solutions are computed at a stoichiometric scalar dissipation rate of  $1 \text{ s}^{-1}$ , where appreciable PAH is present. The PAH mass fraction, surface growth rate coefficient, and oxidation rate coefficient have been normalized to fit on the same scale.

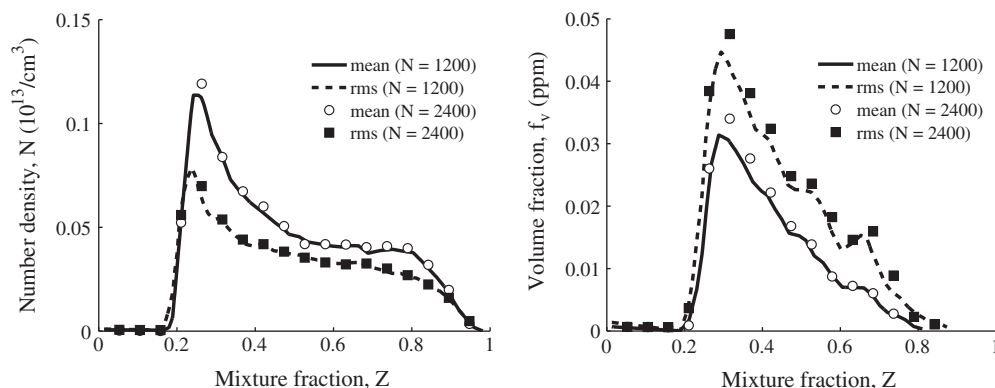


**Fig. 24.** Statistics of soot number density (left) and soot volume fraction (right) conditioned on the local mixture fraction at 15 ms. Statistics for both grid sizes are shown.



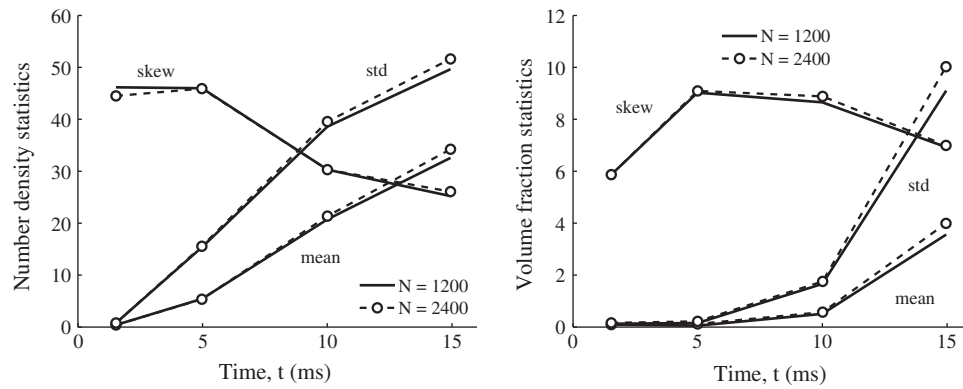


**Fig. 25.** Mean, standard deviation and skewness of soot number density (left) and volume fraction (right) during the simulation at 1.5, 5, 10, and 15 ms. All statistics are rescaled appropriately to fit on the same graph. Results from both grids are shown for comparison.

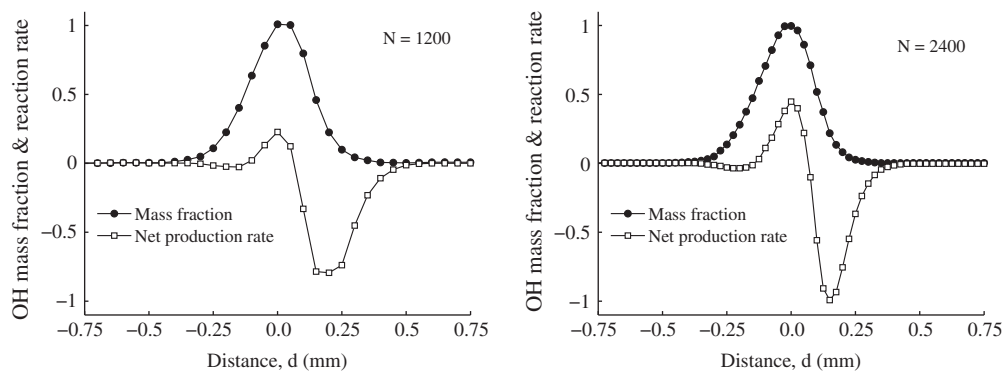


**Fig. 26.** Normalized profiles of the OH mass fraction and OH reaction rate across a flame sheet. The stoichiometric scalar dissipation rate is approximately  $90 \text{ s}^{-1}$ , i.e. 50% of extinction. Data from the  $1200 \times 1200$  (left) and  $2400 \times 2400$  (right) grid simulations is shown for comparison.

remains well localized in mixture fraction space throughout the simulation. Due to the strong sensitivity of PAH to the local dissipation rate, nucleation rates are a function of both mixture fraction and scalar dissipation rate. The concentration of PAH is greatest at locations of large curvature and low scalar dissipation rate, where the resulting nucleation rates are largest. Despite a small bias in favor of transport towards richer mixtures, soot is equally likely to be transported from the nucleation region towards the flame sheet and away from it. This transport bias exists at short simulation times and is gradually reduced as mixing proceeds and the displacement speed becomes positive (mean transport towards the flame). Soot moving towards the flame sheet grows by surface reactions and is oxidized quickly. Conversely, soot moving away from the flame sheet experiences sustained growth due to condensation of PAH on the surface of aggregates. Eventually, most of the soot mass in the domain is localized at compositions richer than those at which soot particles first nucleated. Growth rates of aggregates which are displaced further into the fuel stream diminish rapidly, while the number of primary particles per aggregate increases greatly due to coagulation. Finally, soot mass next to the flame sheet was found to be negligible due primarily to rapid oxidation.

Our results on the formation and early evolution of soot highlight several features having important implications in turbulent sooting flames research and modeling.

- The concentration of PAH is a function of local mixture fraction and scalar dissipation rate. Furthermore, unsteady mixing appears to significantly affect PAH concentration. This behavior explains the observed sensitivity of soot yield to strain rates. These findings emphasize that turbulent combustion models

need to account adequately for the dependence of PAH concentrations on turbulent mixing. In addition, acetylene was shown to be less sensitive to strain. Semi-empirical models using acetylene to describe soot growth are not expected to capture the correct dependency of soot yield on mixing.

- Differential diffusion of soot due to negligible molecular diffusion transport contributes to spreading soot in mixture fraction space. While transport processes are approximately symmetric and movement towards and away from the flame is equally likely at early times, the distribution of soot in mixture fraction space is significantly biased. The highly non-linear growth and destruction processes affecting soot evolution result in soot being preferentially located at mixtures richer than those where particles nucleate.
- The rate of soot mass addition due to nucleation and condensation far exceeds the contribution of surface growth due to the HACA mechanism. Surface reactions are most active next to the flame sheet where soot is oxidized by hydroxyl radicals and molecular oxygen. Soot displaced towards the flame grows by surface reactions and is oxidized quickly. In regions of intense growth, the displacement speed is usually large, leaving little time for growth.
- Soot growth is found to occur at a distance from the flame sheet. Soot displacement at locations of high PAH concentration is found to control the overall soot mass growth rate. Conversely, the movement of soot in the vicinity of the stoichiometric mixture fraction iso-contour [14,15] is considerably less important.
- The morphology of soot particles and aggregates is largely determined by their motion in mixture fraction space. Upon inception, soot particles are small spheres with identical diameters. Aggregates that remain near mixture fraction values

where PAH abound grow further by condensation and nucleation. Their resulting morphology is characterized by the largest primary particles but not the most numerous particles per aggregate. Aggregates that are rapidly displaced toward richer compositions, experience less mass growth and a rapid decrease in number density and corresponding increase in the average number of primary particles per aggregate as coagulation becomes dominant. Small, spherical nucleated particles in regions of persistent nucleation contribute significantly to the number density of particulates, but not to the overall soot volume fraction.

## Acknowledgments

The authors gratefully acknowledge funding from the Strategic Environmental Research and Development Program (SERDP) and the National Aeronautics and Space Administration (NASA). This research was supported in part by the National Science Foundation (NSF) through TeraGrid resources provided by the Texas Advanced Computing Center (TACC) under Grant No. TG-CTS090021. M.E.M. gratefully acknowledges support of the National Defense Science and Engineering Graduate (NDSEG) fellowship program. The authors would like to thank Dr. Pepiot-Desjardins for her help in reducing the chemical mechanism.

## Appendix A. Gas-phase differential diffusion effects

In a sooting turbulent flame, mass transport of species and particulate matter gives rise to two kinds of differential diffusion: (a) differential diffusion between soot and gas-phase species (mixture fraction); and (b) differential diffusion amongst the gas-phase species alone. The importance of the former (soot differential diffusion) has also been recognized in previous works [14,15,62].

Differential diffusion amongst gas-phase species is a secondary effect compared to the differential diffusion between soot and the gas-phase. This is due to the high Schmidt number of soot particles, estimated between 300 and 20,000 (see Section 2.1). Polycyclic aromatic hydrocarbon (PAH) molecules also have a large Lewis number, and their differential diffusion may influence the soot formation process. However, differential diffusion effects for PAH are substantially less important than differential diffusion effects for soot.

Gas-phase Lewis number effects were investigated with the aid of flamelet solutions with constant, non-unity Lewis numbers. Figure 23 compares the steady flamelet solutions for unity Lewis numbers and constant, non-unity Lewis numbers [66]. The inclusion of gas-phase differential diffusion results in a relatively small decrease of the maximum temperature (about 25 K) and a small shift in the location of maximum temperature to a slightly larger mixture fraction. Similar shifts in mixture fraction are seen at the location of maximum surface growth rate coefficient and naphthalene mass fraction. These differences in the gas-phase composition do not appreciably affect the soot evolution.

On the other hand, the inclusion of gas-phase differential diffusion leads to a significant increase in the naphthalene mass fraction (by nearly a factor two). Upon further analysis, this increase was found to be due primarily to the Lewis number of naphthalene and molecular hydrogen. The former results in a direct effect on PAH transport, while the latter results in an indirect effect on hydrogen transport and reaction rates. However, since there are no appreciable absolute or relative shifts in mixture fraction space, the increase in the naphthalene mass fraction acts only to increase the total amount of soot formed in the flame, without changing the dynamics of soot formation.

## Appendix B. Mesh convergence

In order to establish mesh convergence of the soot statistics and soot dynamics, which are the focus of the present paper, a second simulation was performed at twice the resolution: the number of grid points was increased from 1200 to 2400 in both  $x$  and  $y$  directions. Furthermore, the time step size was decreased from 10  $\mu$ s to 5  $\mu$ s. The initial flow field used for the 1200 grid point simulation was interpolated on the finer 2400 point grid, thus allowing for a direct comparison. The main conclusions are presented below.

Figure 24 illustrates the effect of grid refinement on the conditional mean and conditional standard deviation (conditioned on the local value of mixture fraction) of soot number density and volume fraction. We conclude that the statistics are almost identical for the two cases.

Figure 25 shows the evolution in time of mean, standard deviation, and skewness of soot number density and volume fraction. All statistics are rescaled appropriately to fit on the same graph. Largely, the results are identical for the two grids (1200  $\times$  1200 and 2400  $\times$  2400). Some minor differences are apparent for mean and standard deviation towards the end of the simulation (higher for the finer grid).

Figure 26 shows the OH mass fraction and net OH reaction rate profiles across the flame sheet from the two simulations. The flame location is chosen in the flow field so that the stoichiometric scalar dissipation rate is approximately 90  $s^{-1}$ , i.e. 50% of extinction. It is apparent that only five points are found in the half of the each peak (peak production and peak destruction) for the 1200  $\times$  1200 grid. In the case of the 2400  $\times$  2400 grid, it appears that around 10 points are present. The resolution in the case of 1200  $\times$  1200 might seem insufficient to correctly characterize the transport of radical species (e.g. see the discussion in Hawkes et al. [67]). However, mesh refinement by a factor of two did not change soot statistics in any meaningful manner. Hence, even if OH mass fraction may not be quite resolved enough at locations of peak scalar dissipation rate, this bears no consequence on the quantitative and qualitative behavior of soot quantities.

## Appendix C. Supplementary material

Supplementary data associated with this article can be found, in the online version, at doi:10.1016/j.combustflame.2011.05.021.

## References

- [1] H. Bockhorn, Soot Formation in Combustion, Springer-Verlag, New York, 1994.
- [2] K. Donaldson, L. Tran, L.A. Jimenez, R. Duffin, D.E. Newby, N. Mills, W. MacNee, V. Stone, Part. Fibre Toxicol. 2 (2005) 1–14.
- [3] J.S. Lighty, J.M. Veranth, A.F. Sarofim, J. Air Waste Manage. Assoc. 50 (2000) 1565–1618.
- [4] D.X. Du, R.L. Axelbaum, C.K. Law, Proc. Combust. Inst. 22 (1989) 387–394.
- [5] H. Böhm, K. Kohse-Höinghaus, F. Lacas, C. Rolon, N. Darabiha, S. Candel, Combust. Flame 124 (2001) 127–136.
- [6] M. Yamamoto, S. Duan, S. Senkan, Combust. Flame 151 (2007) 532–541.
- [7] J.H. Kent, S.J. Bastin, Combust. Flame 56 (1984) 29–42.
- [8] N.H. Qamar, G.J. Nathan, Z.T. Alwahabi, K.D. King, Proc. Combust. Inst. 30 (2005) 1493–1500.
- [9] C.S. Yoo, H.G. Im, Proc. Combust. Inst. 31 (2007) 701–708.
- [10] C.K. Westbrook, F.L. Dryer, Combust. Sci. Technol. 27 (1981) 31–43.
- [11] J.B. Moss, C.D. Stewart, K.J. Syed, Proc. Combust. Inst. 22 (1988) 413–423.
- [12] P. Narayanan, A. Trouvé, Proc. Combust. Inst. 32 (2009) 1481–1489.
- [13] K.M. Leung, R.P. Lindstedt, W.P. Jones, Combust. Flame 87 (1991) 289–305.
- [14] D.O. Lignell, J.H. Chen, P.J. Smith, T. Lu, C.K. Law, Combust. Flame 151 (2007) 2–28.
- [15] D.O. Lignell, J.H. Chen, P.J. Smith, Combust. Flame 155 (2008) 316–333.
- [16] Z. Qin, V.V. Lissianski, H. Wang, W.C. Gardiner, S.G. Davis, H. Wang, Proc. Combust. Inst. 28 (2000) 1663–1669.
- [17] G. Blanquart, H. Pitsch, in: H. Bockhorn, A. D'Anna, A.F. Sarofim, H. Wang (Eds.), Combustion Generated Fine Carbonaceous Particles, KIT Scientific Publishing, 2009, pp. 437–463.
- [18] F. Williams, Combustion Theory, Perseus Books, New York, 1994.

- [19] H. Pitsch, Flame Master, A C++ computer program for 0D combustion and 1D laminar flame calculations, Technical Report, University of Technology (RWTH), Aachen, 1998.
- [20] S.K. Friedlander, Smoke, Dust and Haze: Fundamentals of Aerosol Behavior, Oxford University Press, New York, 2000.
- [21] R.J. Santoro, T.T. Yeh, J.J. Horvath, H.G. Semerjian, Combust. Sci. Technol. 53 (1987) 89–115.
- [22] O. Desjardins, G. Blanquart, G. Balarac, H. Pitsch, J. Comput. Phys. 227 (2008) 7125–7159.
- [23] M. Herrmann, G. Blanquart, V. Raman, AIAA J. 44 (2006) 2879–2886.
- [24] B.P. Leonard, Comput. Method Appl. Mech. Eng. 19 (1979) 59–98.
- [25] C.D. Pierce, P. Moin, Progress-variable Approach for Large-Eddy Simulation of Turbulent Combustion, Ph.D. thesis, Stanford University, 2001.
- [26] G.D. Byrne, S. Thompson, DVODE F90 support page, 2005. <<http://www.radford.edu/thompson/vodef90web>>.
- [27] R.J. LeVeque, H.C. Yee, J. Comput. Phys. 86 (1990) 187–210.
- [28] G. Strang, SIAM J. Numer. Anal. 5 (1968) 506–517.
- [29] J.C. Butcher, Numerical Methods for Ordinary Differential Equations, Wiley, Chichester, 2008.
- [30] G. Blanquart, P. Pepiot-Desjardins, H. Pitsch, Combust. Flame 159 (2009) 588–607.
- [31] K. Narayanaswamy, G. Blanquart, H. Pitsch, Combust. Flame 157 (2010) 1879–1898.
- [32] J.A. Miller, S.J. Klippenstein, Y. Georgievskii, A. Simmonett, W.D. Allen, in: Proceedings of the 6th US National Combustion Meeting, 2009.
- [33] P. Pepiot-Desjardins, H. Pitsch, Combust. Flame 154 (2008) 67–81.
- [34] R.J. Kee, F.M. Rupley, J.A. Miller, Chemkin-II: a fortran chemical kinetics package for the analysis of gas phase chemical kinetics, Technical Report, SAND-89-8009, Sandia National Labs., Livermore, CA (USA), 1989.
- [35] A. Violi, A. D'Anna, A. D'Alessio, Chem. Eng. Sci. 54 (1999) 3433–3442.
- [36] D. Wong, R. Whitesides, C.A. Schuetz, M. Frenklach, in: H. Bockhorn, A. D'Anna, A.F. Sarofim, H. Wang (Eds.), Combustion Generated Fine Carbonaceous Particles, KIT Scientific Publishing, 2009, pp. 247–257.
- [37] J.S. Bhatta, R.P. Lindstedt, Proc. Combust. Inst. 32 (2009) 713–720.
- [38] S.G. Davis, C.K. Law, Combust. Sci. Technol. 140 (1998) 427–449.
- [39] Y. Huang, C.J. Sung, J.A. Eng, Combust. Flame 139 (2004) 239–251.
- [40] K. Kumar, J.E. Freeh, C.J. Sung, Y. Huang, J. Propul. Power 23 (2007) 428–436.
- [41] S. Jerzembeck, N. Peters, P. Pepiot-Desjardins, H. Pitsch, Combust. Flame 156 (2009) 292–301.
- [42] P. Berta, S.K. Aggarwal, I.K. Puri, Combust. Flame 145 (2006) 740–764.
- [43] A. El-Bakali, J.-L. Delfau, C. Vovelle, Combust. Sci. Technol. 140 (1998) 69–91.
- [44] M.E. Mueller, G. Blanquart, H. Pitsch, Proc. Combust. Inst. 32 (2009) 785–792.
- [45] Ü.Ö. Köylü, G.M. Faeth, T.L. Farias, M.G. Carvalho, Combust. Flame 100 (1995) 621–633.
- [46] M.E. Mueller, G. Blanquart, H. Pitsch, Combust. Flame 156 (2009) 1143–1155.
- [47] M. Frenklach, Chem. Eng. Sci. 57 (2002) 2229–2239.
- [48] D.L. Marchisio, R.O. Fox, Aerosol Sci. 36 (2005) 43–73.
- [49] G. Blanquart, H. Pitsch, Combust. Flame 156 (2009) 1614–1626.
- [50] A.D. Abid, E.D. Tolmachoff, D.J. Phares, H. Wang, Y. Liu, A. Laskin, Proc. Combust. Inst. 32 (2009) 681–688.
- [51] M. Frenklach, H. Wang, Proc. Combust. Inst. 23 (1990) 1559–1566.
- [52] K.G. Neoh, J.B. Howard, A.F. Sarofim, in: D.C. Siegla, G.W. Smith (Eds.), Particulate Carbon, Formation During Combustion, Plenum Press, 1981, p. 261.
- [53] M.E. Mueller, G. Blanquart, H. Pitsch, Proc. Combust. Inst. 33 (2010).
- [54] A. El-Bakali, J.-L. Delfau, R. Akkrich, C. Vovelle, J. Phys. Chem. 94 (1997) 1659–1673.
- [55] H. Böhm, D. Hesse, H. Jander, B. Lüers, J. Pietscher, H.G. Wagner, M. Weiss, Proc. Combust. Inst. 22 (1988) 403–411.
- [56] T. Passot, A. Pouquet, J. Fluid Mech. 181 (1987) 441–466.
- [57] K.A. Buch, W.J.A. Dahm, J. Fluid Mech. 364 (1998) 1–29.
- [58] L.K. Su, N.T. Clemens, J. Fluid Mech. 488 (2003) 1–29.
- [59] H. Pitsch, H. Steiner, Proc. Combust. Inst. 28 (2000) 41–49.
- [60] N. Peters, Prog. Energ. Combust. Sci. 10 (1984) 319–339.
- [61] N. Peters, Turbulent Combustion, Cambridge University Press, 2000.
- [62] H. Pitsch, E. Riesmeier, N. Peters, Combust. Sci. Technol. 158 (2000) 389–406.
- [63] S.B. Pope, Int. J. Eng. Sci. 26 (1988) 445–469.
- [64] E. Van Kalmthout, D. Veynante, Phys. Fluids 10 (1998) 2347–2368.
- [65] T. Echekki, J.H. Chen, Combust. Flame 118 (1999) 308–311.
- [66] H. Pitsch, N. Peters, Combust. Flame 114 (1998) 26–40.
- [67] E. Hawkes, R. Sankaran, J. Sutherland, J. Chen, Proc. Combust. Inst. 31 (2007) 1633–1640.